Agricultural and Forest Meteorology 389 (2026) 111381

Contents lists available at ScienceDirect

Agricultural and Forest Meteorology

journal homepage: www.elsevier.com/locate/agrformet

Disentangling species-specific controls on urban tree transpiration: A Bayesian framework

Xiang Zhang [a,*], Xue Zhong [b], Jun-Ru Yan [c], Qi Li [a,d,e], Ling-Ye Yao [f], Kai-Xin Liu [g], Astrid Moser-Reischl [a], Thomas Rötzer [a], Stephan Pauleit [a], Mohammad A. Rahman [h]

[a] Chair for Strategic Landscape Planning and Management, Technical University of Munich, Emil-Ramann-Str. 6, Freising, 85354, Germany
[b] School of Architecture, Southwest Jiaotong University, Chengdu, 611756, China
[c] College of Horticulture and Landscape Architecture, Southwest University, Chongqing, 400715, China
[d] State Key Laboratory of Subtropical Building and Urban Science, Guangzhou, 510641, China
[e] School of Architecture, South China University of Technology, Guangzhou, 510641, China
[f] School of Architecture, The Chinese University of Hong Kong, New Territories, Hong Kong, China
[g] Institute of Regional Science, Karlsruhe Institute of Technology, Karlsruhe, 76131, Germany
[h] School of Agriculture, Food and Ecosystem Sciences, The University of Melbourne, Burnley, Victoria, 3121, Australia

ARTICLE INFO

Keywords:
Urban microclimate
Bayesian hierarchical modeling
Sap flux density
Jarvis-type model
Species-specific parameterization
Environmental response functions

ABSTRACT

Urban trees regulate water-energy exchanges via transpiration. Although the Jarvis framework is widely used to describe plant physiological responses to environmental drivers, including vapor pressure deficit (*VPD*), solar radiation (R_s), air temperature (T_a), and soil moisture content (θ), key parameter and subfunction structural uncertainties remain insufficiently assessed at the species-specific level. Another challenge is modeling the transpiration variability across multiple sites and seasons simultaneously, particularly in climatically heterogeneous urban settings. Using hourly sap flux density (*SFD*) observations from nine urban sites in Munich and Würzburg, Germany (2015–2021), we fitted 81 subfunction configurations using Markov Chain Monte Carlo (MCMC) Bayesian inference under uniform priors for two species with contrasting wood anatomy: diffuse-porous *Tilia cordata* and ring-porous *Robinia pseudoacacia*. Widely applicable information criterion (WAIC) based Sobol indices quantified structural sensitivity, and species-specific driver sensitivities were reconstructed under the best-performing structure. We then refitted the best Jarvis structure in a hierarchical Bayesian model, treating sites as random effects and adding a seasonal term. Results suggest that (i) at both the parameter and structure levels, the two species exhibit markedly different transpiration responses to environmental drivers, which can be interpreted in relation to known differences in hydraulic architecture and water-use strategy; (ii) model performance is sensitive to subfunction choice rather than increasing monotonically with structural complexity; and (iii) the hierarchical model captures cross-site variation in the transpiration upper bound and improves fit across sites and seasons, with the intraclass correlation coefficient (ICC) exceeding 80% for both species. Collectively, the framework provides uncertainty-aware, species-level Jarvis parameterizations at the single-tree scale, clarifies how species identity and model structure jointly shape sap flux dynamics, and offers an adaptable basis for interpreting and representing species-specific transpiration in urban microclimate models and urban forestry management.

1. Introduction

Urbanization alters land cover and the surface energy balance, leading to persistently higher urban temperatures than in nearby rural areas, a phenomenon known as the urban heat island (UHI) effect (Oke et al., 2017). Combined with increasingly frequent heatwaves, UHI poses a growing challenge to urban climate resilience (Ganguly et al., 2009; Kajosaari et al., 2024). In urban environments, trees mitigate heat through shading and transpiration (Zhang et al., 2022, 2025). Transpiration is an important physiologically regulated component of tree-mediated cooling, as it cools leaves and the canopy boundary layer (Monteith and Unsworth, 2013). Empirical studies have highlighted its cooling potential (Rahman et al., 2018, 2024), with reported reductions

* Corresponding author.
E-mail address: xxiang.zhang@tum.de (X. Zhang).

https://doi.org/10.1016/j.agrformet.2026.111381
Received 10 October 2025; Received in revised form 22 July 2026; Accepted 22 July 2026
Available online 31 July 2026

Abbreviations

SFD	Sap flux density (ml/cm^2/h)
SFD_{max}	Maximum SFD (ml/cm^2/h)
SFD_{norm}	Normalized SFD
SFD^{l}_{max}	Site-specific SFD_{max} (ml/cm^2/h)
$\overline{SFD}_{max}$	Species-level mean SFD_{max} (ml/cm^2/h)
ΔSFD^{l}_{max}	Deviation from $\overline{SFD}_{max}$ (ml/cm^2/h)
l	Site/location index
g_s	Stomatal conductance (m/s)
g_{max}	Maximum g_s (m/s)
R_s	Solar radiation (W/m^2)
$R_{s,max}$	Site-specific maximum R_s (W/m^2)
T_a	Air temperature (°C)
$T_{a,min}$	Minimum T_a for transpiration (°C)
$T_{a,opt}$	Optimal T_a for transpiration (°C)
$T_{a,max}$	Maximum T_a for transpiration (°C)
$k_1 - k_{13}$	Empirical parameters in Jarvis subfunctions
VPD	Vapor pressure deficit (kPa)
θ	Soil moisture content (%)
θ_{def}	Soil moisture deficit
θ_{min}	Site-specific minimum observed θ (%)
θ_{max}	Site-specific maximum observed θ (%)
DOY	Day of year
DOY_{max}	DOY at peak transpiration
DOY_{pre}	Pre-peak seasonal width
DOY_{post}	Post-peak seasonal width
DOY_{window}	Centered DOY window
W	Window length
F^m	Candidate form of the m-th subfunction
$F(R_s)$	Response subfunction for R_s
$F(T_a)$	Response subfunction for T_a
$F(VPD)$	Response subfunction for VPD
$F(\theta)$	Response subfunction for θ
$F(DOY)$	Seasonal response function
$F_i(x_i)$	Response subfunction for x_i
x_i	Environmental variable/driver i
β	Vector of model parameters
O	Set of observed SFD values
j	Observation index
o_j	j-th observed SFD value
n	Number of observations or evaluation points
$\hat{o}_j(\beta)$	Predicted SFD for observation j given β
x_r	r-th evaluation point
α	Multiplicative bias term
σ_{res}^2	Residual variance
σ_{site}	Between-site standard deviation
q_p	p-quantile of a variable
z_i	Normalized environmental driver i
δ_i	Mean absolute hourly increment of z_i
$\Delta_{i,r}$	Point-specific relative perturbation for driver i at evaluation point r
$\overline{E}_i$	Mean absolute log-sensitivity of driver i
w_i	Normalized sensitivity weight of driver i
WAIC	Widely applicable information criterion
ΔWAIC	Difference in WAIC relative to the best model
ΔWAIC%	Percentage increase in WAIC relative to the best model
p_{waic}	Effective number of parameters in WAIC
$\hat{R}$	Potential scale reduction factor
ESS	Effective sample size
S1	First-order Sobol index
ST	Total-effect Sobol index
UHI	Urban heat island
LAI	Leaf area index
TDP	Thermal dissipation probe
HBM	Hierarchical Bayesian model
MCMC	Markov Chain Monte Carlo
NUTS	No-U-Turn Sampler
DIC	Deviance information criterion
elpd	Expected log pointwise predictive density
RMSE	Root mean square error
MAE	Mean absolute error
R^2	Coefficient of determination
CI	Confidence interval
ICC	Intraclass correlation coefficient
SI	Supplementary Information

in city temperatures ranging from 0.5 to 4.0 °C (Anys and Weiler, 2025; Li et al., 2025). However, its cooling contribution varies with environmental and physiological conditions (Rahman et al., 2024), and the interacting controls underlying this variability remain insufficiently resolved in heterogeneous urban settings.

These interacting controls operate along the soil-plant-atmosphere continuum. Stomatal conductance (g_s) responds to vapor pressure deficit (VPD), solar radiation (R_s), air temperature (T_a), and soil moisture content (θ) (Mitchell et al., 2009; Verhoef and Egea, 2014; Wang et al., 2020). For instance, in *Tilia cordata* in Munich, VPD and R_s can individually explain over 50% and 65% of transpiration variability, respectively (Rahman et al., 2017a), while optimal transpiration typically occurs between 20–30 °C, coincident with peak stomatal aperture (Moore et al., 2010). θ often exerts stronger control at seasonal to annual scales, as episodic drought or reduced precipitation limits fluxes (Clausnitzer et al., 2011; Verhoef and Egea, 2014). In urban settings, impervious surfaces, constrained rooting volumes, altered hydrology, and modified urban microclimates further modulate tree water use (Gregg et al., 2003; Gobatti et al., 2025). Even street-canyon configuration can shift transpiration-driven cooling by ~0.4 kW per tree (Rahman et al., 2017a, 2017b). Yet direct in situ measurements remain scarce (Anys and Weiler, 2025), limiting robust cross-site comparison and model evaluation (Rahman et al., 2024).

Recent reviews of urban microclimate models indicate that tree canopy structure and physiology are often simplified, risking omission of key thermal processes (Buccolieri et al., 2018; Yang et al., 2019; (Li et al., 2024b). While shading is widely represented, transpiration-driven cooling can also contribute substantially across neighborhood-to-city scales and should be co-modeled with radiative effects (Zepp et al., 2023; Q. Li et al., 2024; Rahman et al., 2024). Model assessments consequently emphasize the need for reliable species-specific parameterization to improve simulation fidelity (Li and Wang, 2018).

Such parameterization is challenging because of substantial interspecific variation in stomatal regulation, particularly in urban environments characterized by strong heat-water feedbacks (Barros et al., 2019; Fuchs et al., 2021). Tree species exhibit distinct drought strategies rooted in hydraulic architecture (Tabassum et al., 2021; Rahman et al., 2024). For example, diffuse-porous *Tilia cordata* can maintain substantially higher transpiration than ring-porous *Robinia pseudoacacia* under urban conditions (Rahman et al., 2019). Nevertheless, current urban tree transpiration models often rely on generic or species-invariant parameterizations without species-specific calibration, potentially obscuring these physiological contrasts (Li et al., 2024a; Li et al., 2024b).

To represent these environmental controls, Jarvis-type models

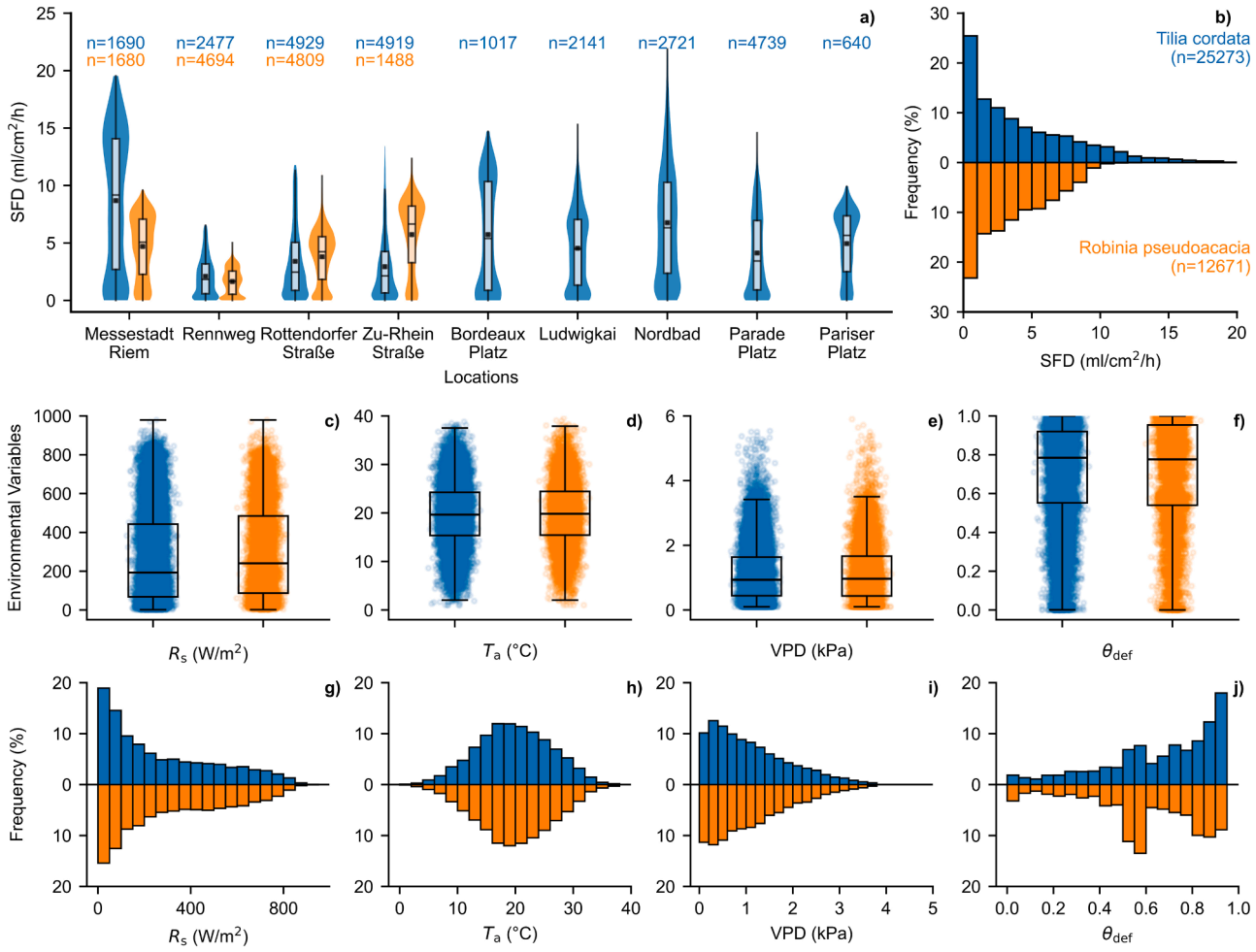

Fig. 1. Data used for model fitting. **a)** and **b)** *SFD* distributions for *T. cordata* (blue) and *R. pseudoacacia* (orange) across nine locations, with overall histograms. **c)** to **f)** Distributions of the four environmental variables (R_s, T_a, *VPD*, θ_{def}), while **g)** to **j)** show the corresponding frequency histograms. Soil moisture deficit is defined as: $\theta_{def} = \frac{\theta_{max}-\theta}{\theta_{max}-\theta_{min}}$, where θ was measured at 30 cm depth, $\theta_{\min}$ and $\theta_{\max}$ are site-specific observed bounds.

(Jarvis, 1976) are widely used to estimate g_s and transpiration from leaves and individual trees to stands and larger domains (Niyogi et al., 2009; Wang et al., 2017; Manickathan et al., 2018, 2020; Chen et al., 2022). The core formulation links an upper-bound term appropriate to the modeled variable (e.g., maximum g_s) with a series of multiplicative environmental response functions, hereafter referred to as subfunctions. Because leaf temperature and leaf water potential are often difficult to observe in field applications, the Stewart modification, which replaces them with *VPD*, R_s, T_a, and θ (Stewart, 1988), has become a widely adopted form.

However, as empirical formulations, Jarvis models face three interrelated sources of uncertainty. First, the upper-bound term is itself uncertain and can vary with age, management, and local microclimate, complicating its specification in urban contexts (Anys and Weiler, 2025). Second, the shapes of the environmental response subfunctions remain largely empirical and non-standard, especially for *VPD*: while stomata generally close with rising *VPD* and are often modeled as linear or exponential declines (Oren et al., 1999), studies show that transpiration may initially rise with *VPD* and subsequently decline beyond a species-specific threshold (Wang et al., 2016; Grossiord et al., 2020). This discrepancy likely reflects differences between leaf-level stomatal regulation and whole-plant hydraulic constraints, and may also arise from differences in experimental systems and parameterization approaches, blurring a universal form. Third, the sensitivity parameters governing responses to environmental drivers are often poorly constrained and species-dependent; for example, species differ in the irradiance at which light responses approach saturation and in the strength of their responses to declining θ (Granier et al., 2007; Feng and Dietze, 2013; Deans et al., 2019). Collectively, these uncertainties limit the generalizability of site-calibrated Jarvis implementations, particularly in heterogeneous urban environments where both species differences and structural choices matter.

These limitations motivate three hypotheses concerning species-specific responses, model-structure sensitivity, and cross-site consistency. (i) If tree species differ in hydraulic architecture and stomatal regulation, then their transpiration responses to *VPD*, R_s, T_a, and θ should be species-specific. (ii) If Jarvis-type models misrepresent these physiological differences by applying inappropriate functional forms, then structural uncertainty will emerge in a species-dependent way, potentially biasing transpiration estimates. (iii) Finally, if the shape of species-specific response functions is governed primarily by intrinsic species characteristics rather than local site effects, then these responses should remain consistent across sites within a shared climatic domain, supporting a shared species-level response structure with site-level random effects. Here, we develop a species-explicit, uncertainty-aware Jarvis framework for urban trees. We use it to quantify species-specific differences in transpiration regulation, test sensitivity to subfunction selection, and evaluate whether hierarchical modeling can represent cross-site and seasonal variation.

2. Materials and methods

The methodological workflow proceeded sequentially: (i) harmonizing site-level datasets through standardized preprocessing; (ii) selecting Jarvis subfunctions and physiologically plausible parameter bounds; (iii) calibrating models at the species level using Bayesian inference; (iv) evaluating parameter and structural uncertainty via sensitivity analysis and alternative subfunction formulations; and (v) applying hierarchical mixed-effects models with species as fixed effects and sites as random effects, further extended with a seasonal response function to capture phenological dynamics. This sequence of calibration, pooling, and sensitivity analysis provides a coherent framework for disentangling species, structure, and site-level influences on transpiration.

2.1. Dataset and processing

Environmental and sap flux data were collected from multiple sites in two major cities of Bavaria, Germany, Munich (48°8′ N, 11°35′ E) and Würzburg (49°48′ N, 9°56′ E), from 2015 to 2021. We monitored 62 mature, healthy street trees across nine locations, focusing on *Tilia cordata* and *Robinia pseudoacacia*, two dominant street-tree species in Bavaria chosen for their contrasting hydraulic strategies: *T. cordata* is diffuse-porous, anisohydric, shade-tolerant, and relatively low in water-use efficiency, whereas *R. pseudoacacia* is ring-porous, isohydric, light-demanding, and highly water-use efficient (Moser-Reischl et al., 2019), enabling species-specific tests of transpiration responses.

Environmental variables used in this study included R_s, T_a, *VPD*, and θ. Sensors were carefully positioned in open areas around focal trees and harmonized across sites. Tree transpiration was quantified using sap flux density (*SFD*, ml/cm^2/h) measured with Granier-type thermal dissipation probes (TDPs; Ecomatik, Dachau, Germany) under standardized protocols applied at all sites (Granier, 1987). All trees were free of visible damage and received no artificial irrigation or pruning during monitoring. Compared to methods relying on gas analyzers or porometers to infer g_s and extrapolate whole-tree transpiration, the TDP approach provides more reliable long-term monitoring at the whole-tree scale.

Fig. 1 summarizes the dataset used for model fitting, covering a broad and typical range of urban environmental conditions across sites and both species; sample sizes vary by site but are representative. To reduce the influence of individual variability and ensure consistency, *SFD* was averaged by species within each site. All variables were aggregated to hourly means. Preprocessing included boxplot-based removal of obvious outliers, retention only of records for which *SFD* and all environmental drivers were temporally aligned, and exclusion of nighttime records ($R_s < 0$). No interpolation or gap-filling was applied; incomplete or non-overlapping observations were excluded from the analysis. Although low levels of nighttime sap flux were observed, existing models rarely capture nocturnal transpiration reliably (Buckley et al., 2012). Even studies that attempt to simulate nighttime fluxes by modifying radiation terms have shown limited accuracy at hourly scales (Wang et al., 2020). As such, this study focuses on transpiration processes occurring during the daytime period.

Additional information on the monitored trees (such as tree age, height, sapwood area, and the number of monitored individuals), together with measurement periods, is provided in the Supplementary Information (SI; Text S1 and Table S1). The underlying datasets and sensor descriptions follow previously published studies (Table S1). For context, Text S1 also summarizes the urban background climate of Munich and Würzburg (mean temperatures, precipitation, and UHI intensity).

2.2. Jarvis model

The Jarvis-type stomatal conductance model is formulated as:

Table 1
Candidate environmental response subfunctions for the Jarvis-type model.

Abbreviations	Subfunctions	References
$F^1(R_s)$	$\frac{R_s \cdot (R_{s,max} + k_1)}{R_{s,max}(R_s + k_1)}$	(Stewart, 1988)
$F^2(R_s)$	$\frac{R_s}{k_2 + R_s}$	(Samanta et al., 2008)
$F^3(R_s)$	$1 - \exp(k_3 \cdot R_s)$	(Kato et al., 2004)
$F^1(T_a)$	$1 - k_4 \cdot (T_{a,opt} - T_a)^2$	(Ortega-Farias et al., 2010)
$F^2(T_a)$	$\left(\frac{T_a - T_{a,min}}{T_{a,opt} - T_{a,min}}\right) \cdot \left(\frac{T_{a,max} - T_a}{T_{a,max} - T_{a,opt}}\right)^{\frac{T_{a,max} - T_{a,opt}}{T_{a,opt} - T_{a,min}}}$	(Stewart, 1988)
$F^3(T_a)$	$\exp\left(-k_5 \cdot \frac{(T_a - T_{a,opt})^2}{T_a + T_{a,opt}}\right)$	(Wang et al., 2020)
$F^1(VPD)$	$\exp\left(\frac{-k_6 (VPD - k_7)^2}{VPD}\right)$	(Wang et al., 2016)
$F^2(VPD)$	$1 - k_8 \cdot VPD$	(Jarvis, 1976)
$F^3(VPD)$	$(1 + k_9 \cdot VPD)^{-1}$	(Samanta et al., 2008)
$F^1(\theta)$	1	-
$F^2(\theta)$	$1 - k_{10} \cdot \exp(k_{11} \cdot \theta_{def})$	(Granier and Loustau, 1994)
$F^3(\theta)$	$\begin{cases} 1, \theta_{def} < k_{12} \\ \left(\frac{k_{13} - 1}{1 - k_{12}}\right)\theta_{def} + \left(\frac{1 - k_{12} \cdot k_{13}}{1 - k_{12}}\right) \end{cases}$	(Poyatos et al., 2007)

$$g_s = g_{max} \cdot F(R_s) \cdot F(T_a) \cdot F(VPD) \cdot F(\theta) \quad (1)$$

Where g_{max} (m/s) denotes the maximum g_s. The four dimensionless response functions (ranging from 0 to 1) represent the constraints imposed by R_s, T_a, *VPD*, and θ, respectively, following the Stewart-type formulation (Stewart, 1988). This multiplicative structure can also be applied to canopy-level transpiration (Whitley et al., 2013), avoiding inverse Penman-Monteith calculations and the need to specify aerodynamic resistance, while noting that aerodynamic effects may still contribute to observed differences in *SFD* across sites. Because stem water storage dynamics (e.g., discharge and refilling processes) cause sub-daily lags between leaf-level transpiration and sap flux (Kume et al., 2008; Wang et al., 2019; Peters et al., 2025), we directly model *SFD* as an indicator of whole-tree transpiration dynamics:

$$SFD = SFD_{max} \cdot F(R_s) \cdot F(T_a) \cdot F(VPD) \cdot F(\theta) = SFD_{max} \prod_{i=1}^{4} F_i(x_i) \quad (2)$$

As previously noted, each $F_i(x_i)$ has multiple candidate forms available in the literature, while the effects of subfunction choice, especially on inferred interspecific differences, remain uncertain. Rather than introducing new physiology, we adopted canonical Jarvis subfunctions. Selection followed a pragmatic logic: to cover the main response shapes while keeping the forms parsimonious and identifiable from hourly *SFD* data, and to preserve comparability across studies. Accordingly, for each driver we considered three candidate forms listed in Table 1 and indexed by the superscript m: saturating responses for light, $F^m(R_s)$; peaked responses (symmetric or asymmetric) for temperature, $F^m(T_a)$; monotonic *VPD* down-regulation or declines beyond a species-relevant threshold, $F^m(VPD)$; and moisture responses including no-limitation and deficit-based limitation, $F^m(\theta)$. Using the same candidate set for both species avoids imposing species differences a priori through the model structure. All 81 combinations, obtained by selecting one of the three forms for each of the four $F_i(x_i)$ terms, were evaluated. The prior specifications are reported in the SI (Text S2 and Table S2).

The parameters k_1 to k_{13}, as well as $T_{a,min}$, $T_{a,opt}$, and $T_{a,max}$ represent empirical constants requiring calibration. $R_{s,max}$ denotes the site-specific maximum R_s, typically assumed to be 1000 W/m^2; $T_{a,min}$, $T_{a,opt}$, and $T_{a,max}$ refer to the minimum, optimal, and maximum T_a for transpiration, respectively.

2.3. Species-specific bayesian calibration

2.3.1. MCMC-based bayesian modeling

The constant parameters in these functional forms determine species-specific transpiration responses. Accordingly, a Bayesian MCMC framework was employed to calibrate these parameters and quantify their posterior uncertainty separately for each species and candidate subfunction combination. Compared to other widely used uncertainty estimation approaches in transpiration modeling (such as the Generalized Likelihood Uncertainty Estimation and the Pareto Optimality), the Bayesian approach provides a coherent probabilistic characterization, allows incorporation of prior knowledge, and supports inference in high-dimensional spaces (Hill, 1974; Samanta et al., 2007, 2008). Accordingly, it is well suited to and widely adopted in Jarvis-type and other transpiration modeling applications (Chen et al., 2020).

The core of Bayesian inference is to update parameter uncertainty by combining priors with data through a likelihood (Zhu et al., 2013). Let $O = o_1,\ o_2, \cdots, o_n$ be the observed *SFD* and $\widehat{o}_j(\beta)$ the model prediction. Assuming independent and identically distributed Gaussian errors with variance ${\sigma_{res}}^2$, the likelihood is:

$$p\left(O|\beta,\ {\sigma_{res}}^2\right) \propto {\sigma_{res}}^{-n} \prod_{j=1}^{n} \exp\left(-\frac{\left(o_j - \widehat{o}_j(\beta)\right)^2}{2{\sigma_{res}}^2}\right) \tag{3}$$

Priors were uniform for β within literature-based feasible ranges and uniform on log $({\sigma_{res}}^2)$, i.e., $p(\beta,\ {\sigma_{res}}^2) \propto \frac{1}{{\sigma_{res}}^2}$ (Zhu et al., 2013), yielding:

$$p\left(\beta,\ {\sigma_{res}}^2|O\right) \propto {\sigma_{res}}^{-(n+2)} \prod_{j=1}^{n} \exp\left(-\frac{\left(o_j - \widehat{o}_j(\beta)\right)^2}{2{\sigma_{res}}^2}\right) \tag{4}$$

Because the posterior has no closed form, we approximated $p(\beta,\ {\sigma_{res}}^2|O)$ via MCMC (Gelman et al., 2013). Specifically, MCMC samples the joint posterior by iteratively proposing parameter values and accepting them with probability given by the posterior ratio (Hastings, 1970). We used the No-U-Turn Sampler (NUTS) in PyMC 4.0, a probabilistic programming package in Python. NUTS is an adaptive Hamiltonian method widely used in modern Bayesian inference because it automatically tunes key sampler parameters during warm-up and typically converges faster than Metropolis-Hastings (Hoffman and Gelman, 2011).

Parameter bounds were compiled from prior studies (SI; Table S2), and the same bounds were used for both species. Within these bounds, priors were weak (i.e., relatively broad) yet physiologically defensible, reflecting established environmental response characteristics reported in the literature, so that inference is data-driven while excluding implausible values. For each of the 81 Jarvis subfunction combinations, we ran four MCMC chains for a total of 8000 iterations, discarding the first half of each chain as warm-up. Convergence was assessed using the potential scale reduction factor ($\widehat{R} < 1.01$), and the effective sample size ($ESS > 400$) (Vehtari et al., 2021). The same specifications and diagnostics were applied independently to *T. cordata* and *R. pseudoacacia* under identical model settings.

2.3.2. Bias adjustment

Although a generic set of environmental stress functions can describe transpiration across seasons and sites, fitting all data in a single MCMC framework often struggles to converge because SFD_{max} varies substantially among sites and over seasons, due to site characteristics, phenology and drought responses (Whitley et al., 2013; Sánchez-Costa et al., 2015; Anys and Weiler, 2025). Prior studies have addressed such heterogeneity by segmenting data seasonally or spatially (Whitley et al., 2013; Wang et al., 2016), but a unified treatment during inference is lacking.

To address this, we first applied a robust, site-wise quantile normalization that sets the local $SFD_{max} \approx 1$ and down-weights extremes (using the 1st to 99th percentiles). Then, a multiplicative bias term α was introduced into the Jarvis structure to absorb systematic, unmodeled variability (including site characteristics and seasonal shifts):

$$SFD_{norm} = \alpha \cdot \prod_{i=1}^{4} F_i(x_i) = \frac{SFD - q_{0.01}(SFD)}{q_{0.99}(SFD) - q_{0.01}(SFD)} \tag{5}$$

We assigned Uniform priors on $[0.5, 1.5]$ for both species. Centered around 1 and constrained to positive values, it permits ±50% departures from the locally normalized amplitude, wide enough to accommodate plausible cross-site and seasonal differences after normalization. This reparameterization improves identifiability and reduces the risk of misattributing variability to particular stress functions. At this stage, the analysis was deliberately constrained to focus on species-specific physiological responses to environmental drivers, while site-specific or seasonal variability was not explicitly modeled. Such structural variance was absorbed into α, allowing the inference process to concentrate on capturing the core Jarvis response structure without conflating environmental sensitivity with unobserved environmental heterogeneity. These additional sources of variability are formally addressed in subsequent sections. Moreover, by combining this structural adjustment with a comprehensive sensitivity analysis, the influence of different environmental drivers and subfunction forms on transpiration modeling was systematically evaluated.

2.3.3. Model training and validation

All data were processed using Python 3.12. For each species, the dataset was randomly split into 70% for training and 30% for validation, with a fixed random seed to ensure reproducibility. For each of the 81 Jarvis subfunction combinations, models were fitted on the training set, and evaluated on the corresponding validation set. Predictive performance was summarized with the coefficient of determination (R^2), root mean square error (RMSE), mean absolute error (MAE), and the widely applicable information criterion (WAIC) (Vehtari et al., 2017). WAIC provides a fully Bayesian estimate of out-of-sample predictive accuracy by approximating the expected log pointwise predictive density (elpd) while integrating over posterior uncertainty (Piironen and Vehtari, 2017). Compared with the Deviance Information Criterion (DIC), widely used in earlier Bayesian studies, WAIC is more robust to highly skewed or multimodal posterior distributions (Gelman et al., 2014), and is standard in modern probabilistic frameworks such as PyMC. Because we employed site-wise quantile normalization and a multiplicative α, scale-based metrics can be confounded by amplitude differences, whereas WAIC evaluates log predictive density and penalizes complexity via the effective number of parameters (p_{waic}), yielding a more likelihood-based and uncertainty-aware comparison across non-nested structures.

2.4. Sensitivity analysis

After completing species-specific Bayesian calibration, each species was associated with a distinct set of calibrated function combinations and parameters. To further explore species-specific variations in Jarvis model behavior, two key aspects were examined: (i) functional sensitivity: whether individual environmental stress functions exhibit species-specific sensitivities, and (ii) structural sensitivity: whether the optimal combinations of subfunctions differ systematically between species. These analyses help elucidate how both the structural configuration and the functional response mechanisms of the Jarvis model reflect interspecific physiological differences.

2.4.1. Species-specific stress responses

To quantify the marginal influence of each environmental driver x_i, the multiplicative Jarvis model was logarithmically transformed into an additive form, enabling partial differentiation with respect to $\ln x_i$:

$$\ln SFD_{norm} = \ln\alpha + \sum_{i=1}^{4} \ln F_i(x_i) \tag{6}$$

Since $\frac{\partial \ln\alpha}{\partial \ln x_i} = 0$, the bias term does not affect sensitivity. Local (pointwise) log-sensitivities were approximated by a central difference in log-space, perturbing x_i by a point-specific relative amount $\Delta_{i,r}$:

$$\left.\frac{\partial \ln SFD_{norm}}{\partial \ln x_i}\right|_{x_r} \approx \frac{\ln F_i\left(x_r(1+\Delta_{i,r})\right) - \ln F_i\left(x_r(1-\Delta_{i,r})\right)}{\ln(1+\Delta_{i,r}) - \ln(1-\Delta_{i,r})} \tag{7}$$

For each species and daytime period (morning: 05–10 h; midday: 10–15 h; afternoon: 15–20 h), drivers were linearly normalized to the species-specific $[q_{0.05},\ q_{0.95}]$ range (Eq. (8a)), and the period-specific step on the normalized series was defined as the mean absolute hourly increment (Eq. (8b)), which was then converted to a pointwise relative perturbation ($\Delta_{i,r}$) on the original scale at the evaluation grid point (Eq. (8c)):

$$z_i = \frac{x_i - q_{0.05}}{q_{0.95} - q_{0.05}} \in [0,1] \tag{8a}$$

$$\delta_i = \overline{|z_i(t+1) - z_i(t)|},\ \Delta t = 1h \tag{8b}$$

$$\Delta_{i,r} = \delta_i \frac{q_{0.95} - q_{0.05}}{x_r} \tag{8c}$$

Where the overbar denotes averaging over all valid hourly steps within the period. This data-driven definition makes δ_i reflect the observed, time-varying rate of change in each environmental driver, capturing diurnal heterogeneity (e.g., larger δ_{Rs} in the morning when irradiance rises rapidly and smaller around midday when it stabilizes). Estimating δ_i separately by species and period and averaging within period yields a representative step that is physiologically meaningful and numerically stable while limiting undue influence from transient spikes. The mean absolute log-sensitivity $\overline{E}_i$ over the typical domain was estimated via numerical integration using n equally spaced evaluation points:

$$\overline{E}_i = \frac{1}{\ln q_{0.95} - \ln q_{0.05}} \int_{\ln q_{0.05}}^{\ln q_{0.95}} \left|\frac{\partial \ln F_i}{\partial \ln x_i}\right| d(\ln x_i) \tag{9a}$$

$$\ln x_r = \ln q_{0.05} + (r-1)\frac{\ln q_{0.95} - \ln q_{0.05}}{n-1},\ r \in [1,2,\ldots,n] \tag{9b}$$

Here, x_r denotes the r-th evaluation point on the logarithmic grid spanning $[q_{0.05},\ q_{0.95}]$. The pointwise $\Delta_{i,r}$ used in Eq. (7) is computed at each x_r from δ_i via Eq. (8c). This yields the discrete approximation:

$$\overline{E}_i \approx \frac{1}{n}\sum_{r=1}^{n} \left|\frac{\ln F_i\left(x_r(1+\Delta_{i,r})\right) - \ln F_i\left(x_r(1-\Delta_{i,r})\right)}{\ln(1+\Delta_{i,r}) - \ln(1-\Delta_{i,r})}\right| \tag{10}$$

To enable cross-variable comparison, sensitivities were normalized to sum to unity, representing the proportionate influence of each environmental driver under the model parameterization and observed range:

$$w_i = \frac{\overline{E}_i}{\overline{E}_{Rs} + \overline{E}_{Ta} + \overline{E}_{VPD} + \overline{E}_{\theta}} \tag{11}$$

Uncertainty was quantified via a double-bootstrap: (i) parameter uncertainty by sampling Jarvis parameters from the full MCMC posterior, and (ii) data uncertainty by resampling the observed x_i series within each species and period. This resampling draws from the entire seasonal record available for that species and period, so the resulting sensitivity distributions integrate over seasonal variability in the environmental drivers. The procedure was repeated 1000 times, yielding empirical distributions from which 95% confidence intervals (CI) were derived, following common bootstrap-based uncertainty reporting for sensitivity indices (Nossent et al., 2011).

2.4.2. Species-specific subfunction combinations

Selecting appropriate subfunctions is harder than tuning parameters within a fixed form. Although various formulations for subfunctions have been proposed, a systematic evaluation of their suitability for different tree species remains absent. We therefore quantified structural sensitivity (Kelleher et al., 2013; Van Hoey et al., 2014) by analyzing the WAIC across 81 Jarvis configurations for two species. We then applied a Sobol variance-based global sensitivity analysis to these WAIC values, treating the chosen subfunction for each driver ($F(R_s)$, $F(T_a)$, $F(VPD)$, $F(\theta)$) as an input factor with three levels. Sobol analysis decomposes the across-configuration variance of WAIC into contributions from each factor and their interactions. We report first-order (S1, variance attributable to one driver's subfunction choice averaged over the others) and total-effect (ST, that driver's main effect plus all interactions) indices, with pairwise interactions summarized where informative (Sobol', 2001). The "variance being evaluated" is the variability in WAIC caused by swapping subfunctions across the 81 structures (with parameters re-estimated each time), not random noise from a single fit. Using WAIC as the metric ensures a fully Bayesian comparison that balances fit and effective complexity while integrating posterior uncertainty, so the Sobol decomposition isolates between-structure effects driven by subfunction specification and reveals which driver's choice most affects predictive performance, and whether these sensitivities are species-specific.

Uncertainty in the Sobol indices was quantified by bootstrapping the WAIC estimates. In 1000 iterations, for each configuration we drew WAIC from a normal distribution with the MCMC-estimated mean and standard error, recomputed the indices, and obtained 95% CIs. The details of the Sobol index computation are provided in the SI (Text S3).

2.5. Formalizing site and seasonal effects

Based on the species-specific optimal Jarvis configurations and the cross-species comparisons of parameter and structural sensitivities, we further decomposed the previously introduced α into a site effect and a seasonal component for the formal model. All subsequent analyses used the original unscaled *SFD* to preserve physical units and enable direct comparison with field observations. All other Jarvis parameters retained the same literature-based bounds, MCMC settings, and convergence diagnostics as in the species-specific fits.

2.5.1. Site-level hierarchical modeling

To represent spatial heterogeneity, we refit the model as a hierarchical Bayesian model (HBM) (Clark, 2005), conditional on the species-specific optimal Jarvis structure selected above (i.e., one fixed subfunction combination per species). Species is treated as a fixed effect (through separate species-level parameters), whereas sites are random effects that partially pool site estimates. Under Hypothesis 3, the $F_i(x_i)$ encode species-level sensitivities that are approximately invariant across sites within a shared climatic domain; in urban settings, spatial heterogeneity is expected primarily to scale the magnitude of sap flux (capacity) rather than reshape short-term response curves. Accordingly, we represent site heterogeneity solely via a random intercept on SFD_{max} (with no random slopes on $F_i(x_i)$), since adding random slopes would conflate site effects with driver sensitivities, greatly increase dimensionality, and be weakly identified. Here "site" includes both location and individual-tree differences. Because *SFD* was averaged by species within each site, the site random intercept absorbs (i) site-level factors (such as surface sealing, rooting volume, exposure/microclimate, and management) and (ii) unmodeled individual variability (such as age, DBH, height, crown architecture, and sapwood area). Conceptually, the earlier α acted as a capacity scaler; the HBM formalizes the same idea as a random intercept on SFD_{max}. Each site-specific SFD^{l}_{max} was modeled as:

$$SFD^{l}_{max} \sim \mathcal{N}\left(\overline{SFD}_{max},\ \sigma_{site}\right) \tag{12}$$

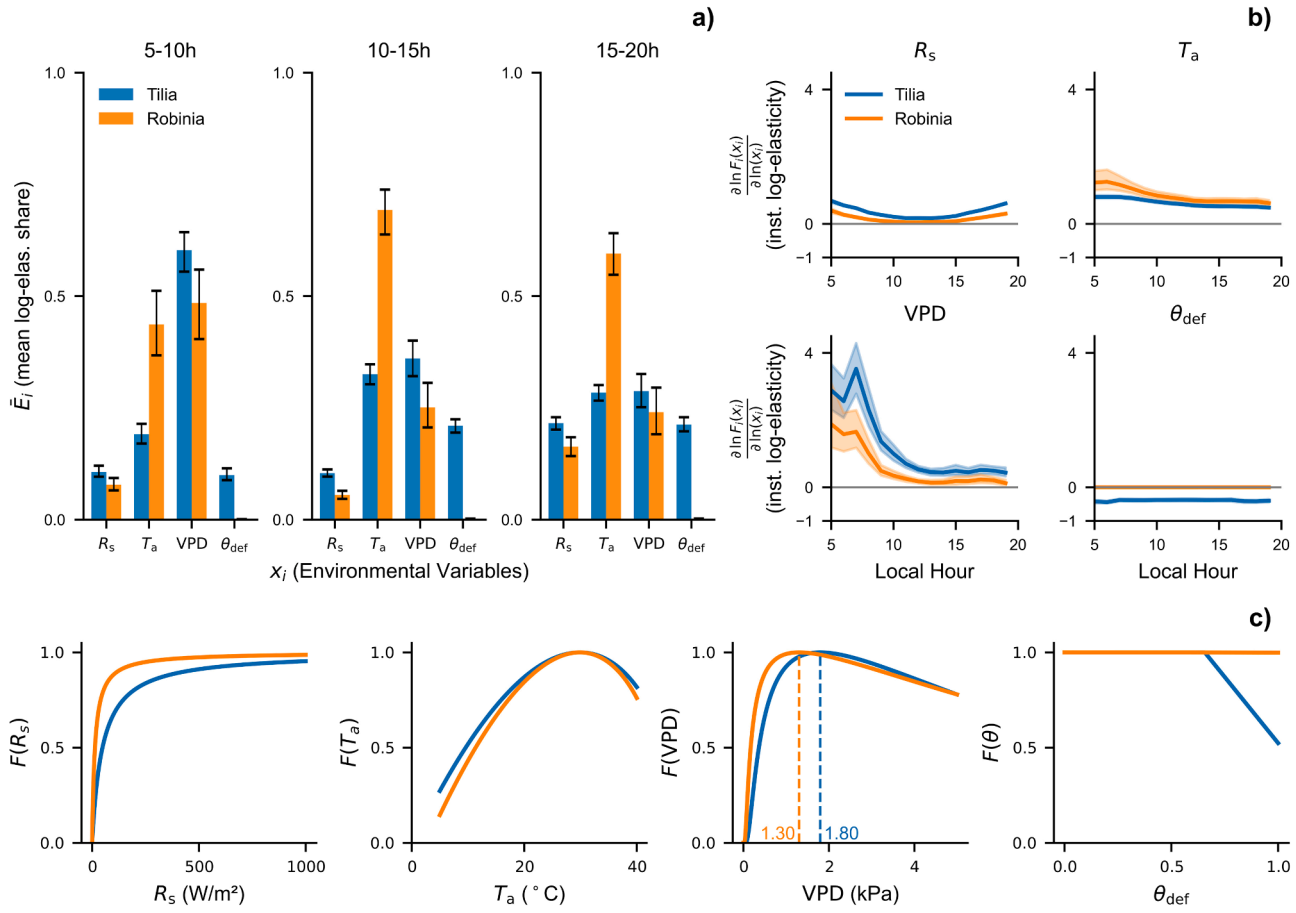

Fig. 2. **a)** Mean hourly sensitivities (log-elasticities) of four environmental variables (R_s, T_a, *VPD*, and θ_{def}) for two species (blue: *T. cordata*, orange: *R. pseudoacacia*) during three daytime intervals (5–10 h, 10–15 h, and 15–20 h). Error bars represent 95% CI derived from the double-bootstrap procedure, combining parameter uncertainty from the Bayesian posterior with data uncertainty from resampling the observed driver series. **b)** Instantaneous log-elasticity ($\frac{\partial \ln F_i(x_i)}{\partial \ln(x_i)}$) dynamics for each environmental variable across local time, illustrating the temporal evolution of each variable's influence on the Jarvis response function for both species. Solid lines denote the mean value, and shaded bands indicate the corresponding 95% CI derived from the same double-bootstrap procedure; each subplot corresponds to a specific driver. **c)** Best-fit functional forms of the Jarvis model subfunctions for *T. cordata* ($F^2(R_s)\cdot F^2(T_a)\cdot F^1(VPD)\cdot F^3(\theta)$) and *R. pseudoacacia* ($F^2(R_s)\cdot F^2(T_a)\cdot F^1(VPD)\cdot F^1(\theta)$). Dashed lines highlight inflection points in the *VPD* subfunction.

Where $\overline{SFD}_{max}$ is the species-level mean and σ_{site} is the between-site standard deviation. The half-normal prior (scale 5) ensures non-negativity for σ_{site} while remaining weakly informative, as it is broad enough to allow for substantial between-site variability yet consistent with empirical observations that cross-site differences in SFD^l_{max} rarely exceed 10 ml/cm^2/h. The half-normal form also promotes numerical stability for variance components and is widely recommended when the number of groups is small (Gelman, 2006), consistent with our study design (nine sites for *T. cordata*, and four for *R. pseudoacacia*). In addition, we computed the intraclass correlation coefficient (ICC) to quantify the proportion of total variance attributable to between-site differences:

$$ICC = \frac{\sigma^2_{site}}{\sigma^2_{site} + \sigma^2_{res}} \tag{13}$$

Where σ^2_{res} is the residual variance. Thus, the ICC represents the share of total variance in SFD^l_{max} attributable to site-level heterogeneity; values near 1 indicate dominance of between-site differences, whereas values near 0 indicate that variability is primarily within sites.

2.5.2. Seasonal adjustment function

Subsequently, we incorporated a seasonal function as an additional subfunction in the Jarvis model. In some studies utilizing inverted Penman-Monteith formulations, seasonal variations in transpiration were represented through the calibration of leaf area index (LAI) (Chen et al., 2020). However, as a structural canopy descriptor, it cannot capture whole-tree physiological changes across phenological phases (e.g., leaf age distribution, stomatal aging, dormancy), and thus underrepresents seasonal dynamics (Damour et al., 2010). A further challenge is specifying a priori temporal rules for empirical parameters (Damour et al., 2010). To address this, we introduced an empirical seasonal response $F(DOY)$ for temperate deciduous species with winter dormancy:

$$F(DOY) = \begin{cases} \exp\left(-\frac{(DOY - DOY_{max})^2}{2DOY_{pre}{}^2}\right), DOY \le DOY_{max} \\ \exp\left(-\frac{(DOY - DOY_{max})^2}{2DOY_{post}{}^2}\right), DOY > DOY_{max} \end{cases} \tag{14a}$$

$$DOY_{window} = \left\lfloor \frac{DOY}{W} \right\rfloor \cdot W + \frac{W}{2} \tag{14b}$$

Where DOY_{max} is the day of peak *SFD*. Separate pre- and post-peak widths (DOY_{pre}, DOY_{post}) allow asymmetry. Because seasonal processes do not operate at hourly or daily scales, we aggregated data into non-overlapping 15-day windows (Eq. (14b)) to suppress high-frequency noise and improve parameter identifiability and MCMC convergence. Moreover, because the dataset aggregates multiple sites and years, with occasional gaps, we aim to capture the within-year envelope of

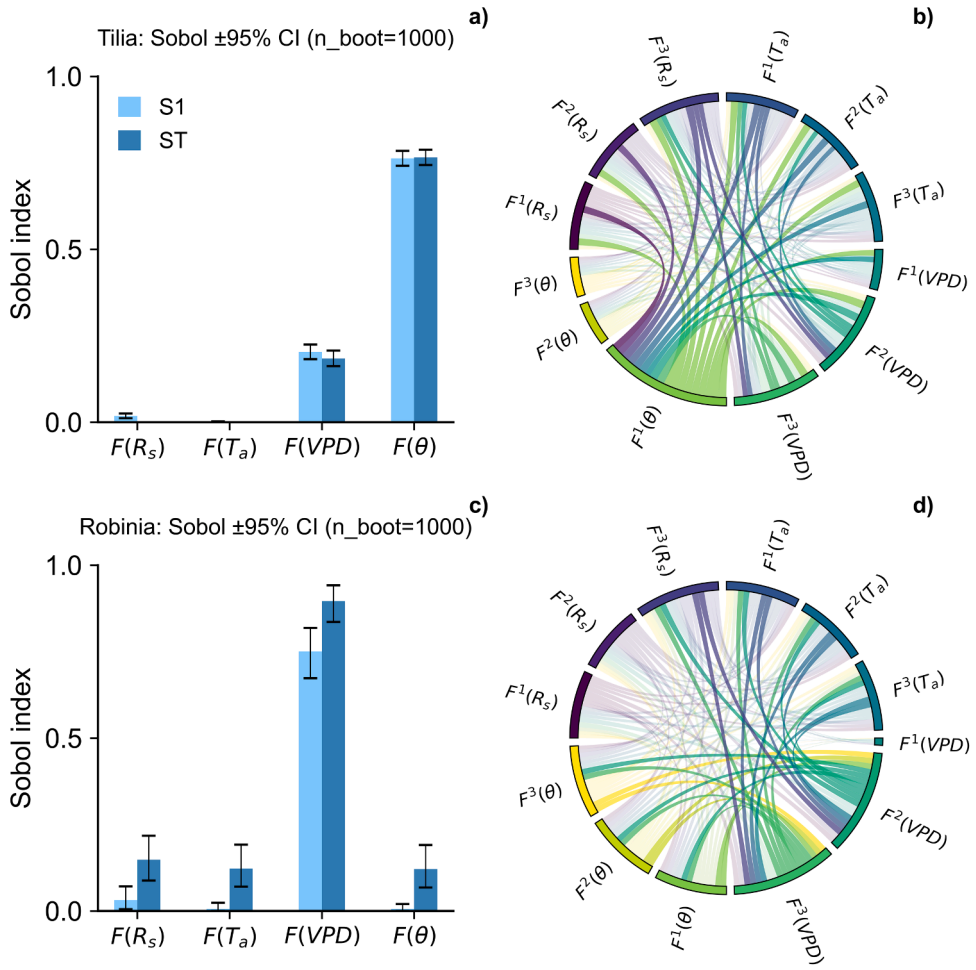

Fig. 3. a) and **c)**: WAIC-based Sobol indices for Jarvis subfunctions (S1: first-order; ST: total effect, error bars show 95% bootstrap CI) for *T. cordata* and *R. pseudoacacia*. **b)** and **d)**: ΔWAIC% chord diagrams summarizing model-structure co-dependence. Here, ΔWAIC% is the percentage increase in WAIC relative to the best model when a single subfunction is replaced (lower WAIC means better fit). Arc length is proportional to the median ΔWAIC% for that subfunction; longer arcs indicate larger expected deterioration if it is mis-specified. Chord width reflects the median joint deterioration when two subfunctions are mis-specified together. For clarity, only the top 20% strongest links are shown.

transpiration rather than site-specific phenological dates. In Central Europe, *T. cordata* and *R. pseudoacacia* typically initiate leaf-out or active transpiration during April-May and cease by mid-October, with summer (June-August) hosting the seasonal maximum (Moser-Reischl et al., 2019; Rötzer et al., 2021; Anys and Weiler, 2025; Moser-Reischl et al., 2025). Accordingly, the bounds are common to both species: we place a Uniform prior on DOY_{max} with support $[100, 270]$, and weak, wide Uniform priors on DOY_{pre} and DOY_{post} with support $[50, 250]$. The 50-day lower bound accommodates an approximately two-month ramp from leaf-out (April) to early-summer peaks (Moser-Reischl et al., 2025), and the broad 250-day upper bound captures the typically more gradual autumn decline (Rötzer et al., 2021).

3. Results

3.1. Performance and sensitivities of species-specific Jarvis models

After running MCMC for all 81 Jarvis subfunction configurations, the species-specific optima were selected based on WAIC ranking: *T. cordata* ($R^2 = 0.55$, RMSE = 0.19, MAE = 0.14) and *R. pseudoacacia* ($R^2 = 0.46$, RMSE = 0.21, MAE = 0.17), and the fitted α was 0.87 and 0.72, indicating modest residual amplitude down-scaling after site-wise quantile normalization; α rescales magnitude but does not affect the selected subfunction shapes or the WAIC-based ranking. Both species share the same forms for $F^2(R_s)\cdot F^2(T_a)\cdot F^1(VPD)$, and differ only in the θ term: *T. cordata* favors $F^3(\theta)$ whereas *R. pseudoacacia* is best captured by $F^1(\theta)$, implying its negligible apparent sensitivity to near-surface θ_{def} under the observed range (Fig. 2c). All configurations met convergence criteria; summary metrics for all alternatives are provided in the Supplementary Data, while detailed convergence diagnostics and posterior distributions are reported for the best-performing model of each species (SI; Tables S3-S4).

The fitted $F(T_a)$ suggests a similar thermal optimum near 30 °C for both species, while *R. pseudoacacia* reaches light saturation at lower R_s, and exhibits a narrower $F(T_a)$ parabola. In the $F(VPD)$, the downturn occurs later for *T. cordata* (inflection≈1.8 kPa), and earlier for *R. pseudoacacia* (inflection≈1.3 kPa), consistent with earlier stomatal regulation under increasing atmospheric dryness.

Sensitivity analysis is consistent with these patterns. Hourly mean log-elasticities (Fig. 2a) show pronounced early-morning sensitivity to *VPD* (5–10 h) in both species, followed by a midday reduction in R_s elasticity once light saturation is approached (10–15 h) and a concomitant rise in T_a elasticity, stronger in *R. pseudoacacia*. Instantaneous sensitivity (Fig. 2b) reveals a transient post-sunrise peak in *VPD* responsiveness, driven by the rapid increase in R_s and T_a prior to full stomatal regulation, and a subsequent decline as control tightens. Across the daytime (5–20 h) θ exerts minimal influence at hourly scales. This does not preclude sensitivity under more severe drought or at deeper soil

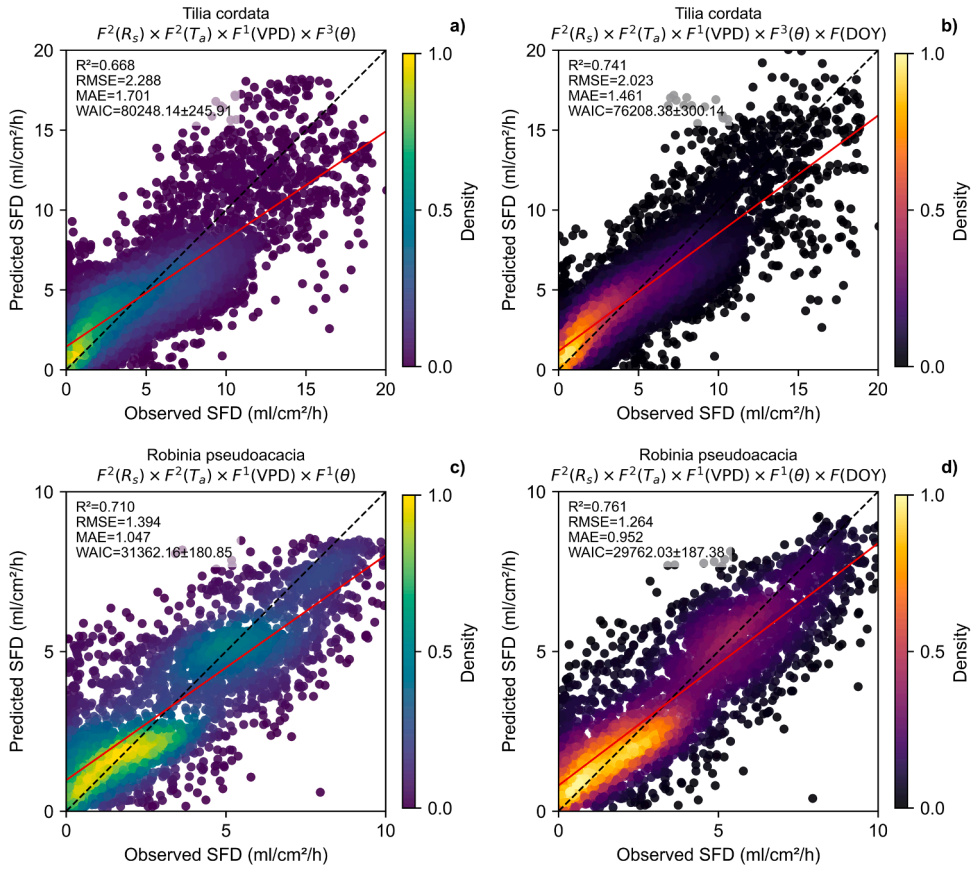

Fig. 4. Observed-predicted comparisons for *SFD* under the species-specific optimal Jarvis configuration. **a)** and **c)** hierarchical Bayesian models with location-level random effects; **b)** and **d)** the same models augmented with a seasonal term $F(DOY)$. Species: *T. cordata* **(a, b)** and *R. pseudoacacia* **(c, d)**. Points are shown with density shading; the dashed diagonal indicates the 1:1 line. Model performance is evaluated using R^2, RMSE (ml/cm^2/h), MAE (ml/cm^2/h), and WAIC.

layers.

3.2. Species-specific structural sensitivity of Jarvis subfunctions

The 81 Jarvis subfunction combinations were evaluated under a unified set of priors for both species. Fig. 3a and c report WAIC-based Sobol indices. Rather than listing second-order Sobol terms, Fig. 3b and d use a ΔWAIC% chord diagram to visualize structural co-dependence in performance deterioration: a longer arc for a given subfunction means that replacing it tends to produce a larger ΔWAIC (i.e., a worse fit). For both species, altering the $F(T_a)$ and $F(R_s)$ contributes negligibly, indicating that within the chosen prior ranges and data domain, altering their functional forms has little impact.

In *T. cordata*, performance is most sensitive to $F(\theta)$, followed by $F(VPD)$, with the poorest fits consistently associated with $F^1(\theta)$; moreover, S1≈ST across all subfunctions, indicating that model performance is largely governed by independent main effects rather than cross-driver interactions (Fig. 3a and b). In *R. pseudoacacia*, sensitivity concentrates in $F(VPD)$; interestingly, combinations including the rise-decline $F^1(VPD)$ consistently achieve the best scores, whereas monotonic-decay forms perform poorly, implying that such forms fail to capture the initial increase in transpiration within our domain, thereby yielding large WAIC penalties (Fig. 3c and d). Moreover, *R. pseudoacacia* exhibits stronger higher-order interactions, with ST>S1 across drivers, indicating that interactions play a larger role in predictive performance than main effects; model performance depends more on cross-driver combinations than on any single subfunction.

3.3. Hierarchical Bayesian modeling incorporating location and seasonal effects

Using the original *SFD* units (ml/cm^2/h), hierarchical Bayesian models built on the species-specific optimal Jarvis structures performed well for both species (Fig. 4a and c). Compared with *R. pseudoacacia, T. cordata* exhibits a broader dynamic range, with occasional values up to 15–20 ml/cm^2/h. Nevertheless, for both species most observations lie within 10 ml/cm^2/h. Adding the $F(DOY)$ further improved performance (Fig. 4b and d): for *T. cordata*, R^2 increased by 10.9%, while RMSE, MAE, and WAIC decreased by 11.6%, 14.1%, and 5.0%; for *R. pseudoacacia*, R^2 increased by 7.2%, and RMSE, MAE, and WAIC decreased by 9.3%, 9.1%, and 5.1%. These improvements indicate that combining partial pooling with explicit seasonal modulation accommodates *T. cordata*'s larger seasonal amplitude particularly well, while still delivering consistent improvements for *R. pseudoacacia*. Detailed convergence diagnostics and posterior parameter distributions for the hierarchical models, without (Tables S5-S6) and with $F(DOY)$ (Tables S7-S8) are provided in the SI.

The fitted $F(DOY)$ curves differ sharply by species (Fig. 5a). *T. cordata* rises steeply and peaks early (April to May); the decline begins near *DOY* 136, and by *DOY* 300 the response is ~25% of its peak. *R. pseudoacacia* increases more gradually, peaks later (August to September; decline onset ~*DOY* 266), and retains a large fraction of its peak, indicating a more prolonged active period.

Fig. 5b shows that site effects are strong for both species but larger for *T. cordata*, with typical absolute deviations (ΔSFD^l_{max}) reaching 0–10 ml/cm^2/h (occasionally higher), whereas *R. pseudoacacia* varies on the order of 0–5 ml/cm^2/h. The ICC indicates that 90% (*T. cordata*) and 80% (*R. pseudoacacia*) of the variance in SFD^l_{max} is attributable to

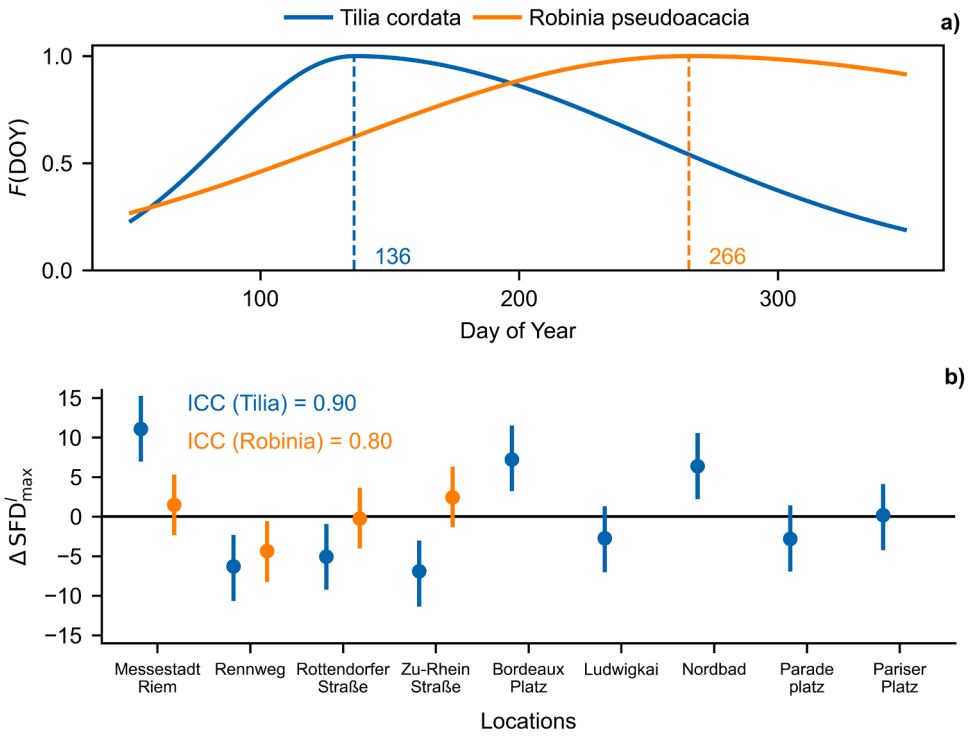

Fig. 5. Seasonal and spatial patterns of *SFD* for *T. cordata* (blue) and *R. pseudoacacia* (orange). **a)** Fitted $F(DOY)$, with vertical dashed lines indicating the *DOY* at which *SFD* begins to decline. **b)** Between-site variation in ΔSFD^{l}_{max} calculated as $SFD^{l}_{max} - \overline{SFD}_{max}$, representing each location's deviation from the species-specific mean. Points denote posterior means and whiskers indicate 95% highest density intervals of the posterior distributions. ICCs quantify the proportion of variance in SFD^{l}_{max} attributable to between-site differences.

between-site differences, i.e., strong spatial structuring within species.

3.4. Hourly sap flux simulations at representative locations

To minimize artifacts from gaps or outliers and to ensure broad temporal coverage, we display windows with the most complete and continuous hourly records drawn from distinct parts of the year. The band broadens near peak *SFD*, indicating greater predictive variance at high flux. The model also reproduces abrupt, environmentally forced transitions (e.g., *DOY* 198–199 in Fig. 6a; *DOY* 261–264 in Fig. 7c). Minor underestimation appears at extreme midday peaks under clear, high *VPD* conditions, but overall coverage and timing remain robust. Notably, *T. cordata* shows a pronounced seasonal attenuation of *SFD* (Fig. 6c and f), whereas *R. pseudoacacia* maintains a comparatively stable amplitude across the displayed periods.

4. Discussion

4.1. Species-specific patterns in Jarvis parameters and model structure

Across nine Central-European urban sites, the two species showed species-specific patterns of transpiration control within the Jarvis framework. Consistent with prior work, daytime *SFD* is dominated by atmospheric drivers, especially *VPD* (Huang et al., 2011; Rahman et al., 2017a; Anys and Weiler, 2025). However, *R. pseudoacacia* shows an earlier *VPD* downturn and weak θ sensitivity, whereas *T. cordata* appears to sustain higher flux under higher *VPD* yet exhibits stronger θ penalties.

Importantly, although these fitted response patterns do not mechanistically resolve internal tree water transport, they are consistent with known differences in hydraulic architecture and water-use strategy between the two species. Ring-porous *R. pseudoacacia* (with larger earlywood vessels and higher embolism vulnerability) may initiate stomatal regulation earlier under rising *VPD*, whereas diffuse-porous *T. cordata* appears to maintain transpiration to higher *VPD* (Tyree and Ewers, 1991; Moser-Reischl et al., 2019; Rötzer et al., 2021; Torres-Ruiz et al., 2024; Moser-Reischl et al., 2025). Differences in $F(\theta)$ may reflect contrasting water-access pathways rather than functional flexibility alone. In urban environments, shallow θ at 30 cm depth may not fully represent rooting-zone water availability, especially for *R. pseudoacacia*, for which reported deep rooting and possible access to deeper water or groundwater may partially decouple measured θ from actual tree water status (Zhou et al., 2022). The weaker apparent θ sensitivity of *R. pseudoacacia* should be interpreted as a response to measured topsoil moisture under the monitored conditions rather than a fully resolved rooting-zone water-stress function, whereas *T. cordata* may remain more exposed to near-surface deficits.

Beyond water regulation, the fitted light and temperature responses also differ: *R. pseudoacacia* shows a rapid increase in the fitted light response with increasing R_s, consistent with its reported sensitivity to light (Cierjacks et al., 2013). Its small pinnate compound leaves may also enhance convective coupling and allow leaf temperature to track T_a more closely (Leigh et al., 2017), which could contribute to the stronger apparent role of T_a around midday as $F(VPD)$ elasticity declines.

4.2. Seasonality and location-level heterogeneity of transpiration

Significant cross-site differences in SFD_{max} were observed. Because the Jarvis upper bound is often proxied by site maxima (Mackay et al., 2012; Wang et al., 2020), directly pooling multi-site data can destabilize fits when upper limits diverge. Relative to the prior five-site Jarvis study in Australia (Whitley et al., 2013), which showed that a common set of environmental-response families can be used across sites after re-estimating maximum transpiration, we adopt the same separable structure but do not re-tune subfunctions by site: subfunctions are fixed at the species level, and between-site heterogeneity is accommodated only via a hierarchical SFD_{max}. The resulting robust fits are consistent with hypothesis 3. Whitley et al. also reported that $F(\theta)$ could be difficult to identify at some sites; in our urban network we quantify topsoil

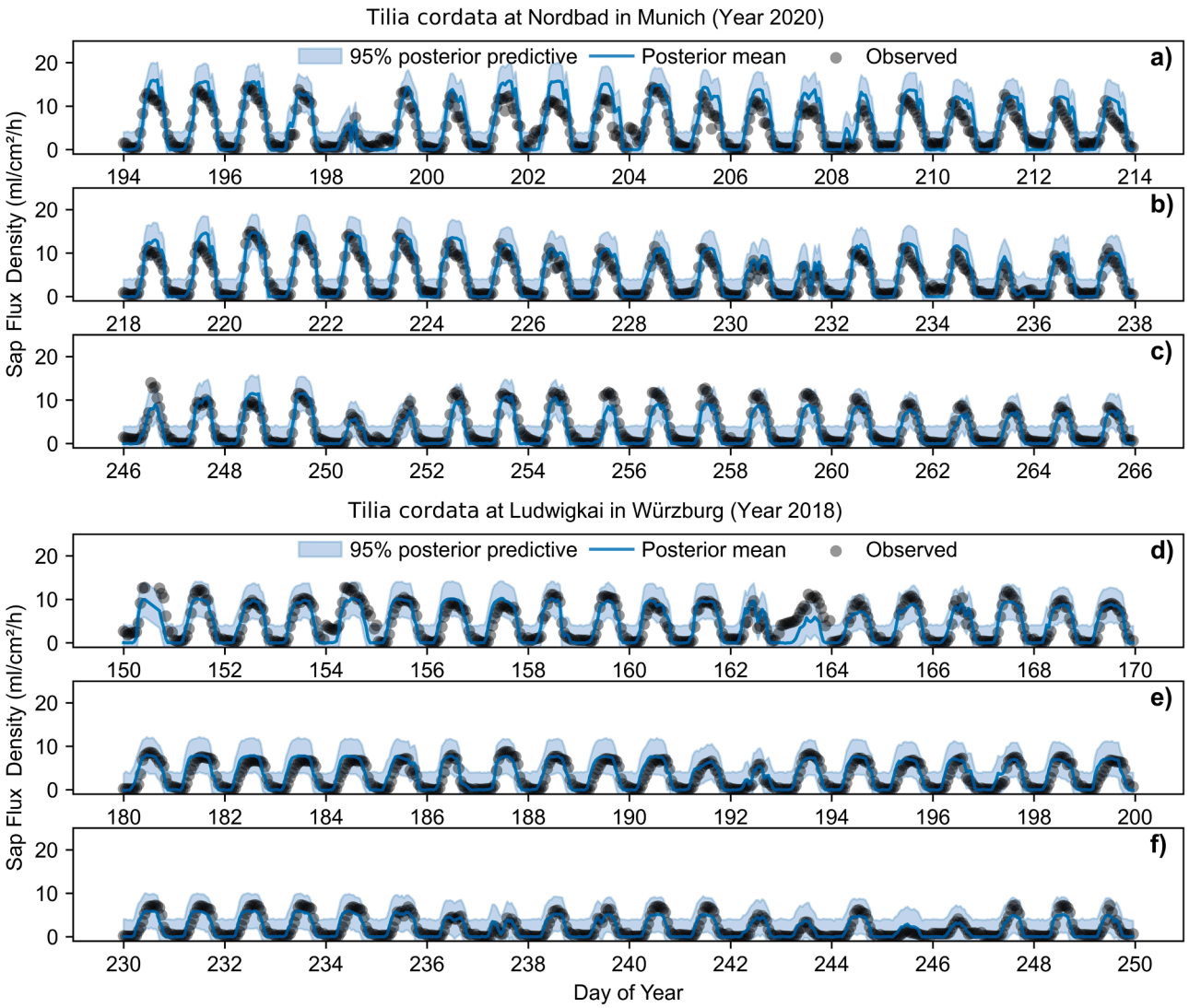

Fig. 6. Posterior predictive distributions of *SFD* for *T. cordata*, generated using an HBM with the optimal Jarvis configuration: $F^2(R_s)\cdot F^2(T_a)\cdot F^1(VPD)\cdot F^3(\theta)\cdot F(DOY)$. Each panel shows a selected continuous window: posterior predictive mean (solid line), 95% posterior predictive interval (shaded), and the observations (points). The 95% posterior predictive interval is the 2.5th-97.5th percentile range of the posterior predictive distribution.

constraint using a θ_{def} rather than absolute moisture, improving comparability under differing soil physical properties.

Residual amplitude differences are plausibly associated with site heterogeneity, including surface sealing, soil physical conditions, rooting volume, and tree structural differences such as size and age (Kjelgren and Clark, 1992; Schäfer et al., 2000; Delzon and Loustau, 2005; Rahman et al., 2019; Anys and Weiler, 2025). Because these effects are substantial in urban settings but difficult to parameterize directly, the hierarchical treatment improves prediction across heterogeneous sites while preserving a common species-level response structure, but it does not identify their causal mechanisms.

Seasonal fits suggest that the relative early-late phase ordering is more informative than a precise *DOY* estimate. This timing may reflect their diffuse- vs. ring-porous anatomy and associated phenology: diffuse-porous *T. cordata* can resume water transport on previous-year xylem, enabling earlier leaf-out in spring and typically earlier senescence, while ring-porous *R. pseudoacacia* must produce new earlywood to replace winter-embolized conduits, delaying leaf-out to late May to June and often prolonging canopy activity into early autumn (Panchen et al., 2014; Moser-Reischl et al., 2019). These phenological phase shifts may reshape seasonal transpiration and support the explicit representation of seasonality in multi-species transpiration models. LAI seasonality alone may not fully capture such timing differences, because canopy development can lag behind the recovery or loss of hydraulic function (Paschalis et al., 2024).

4.3. Uncertainty in Jarvis subfunctions

Across the 81 subfunction configurations for each species, WAIC-based Sobol indices and ΔWAIC show that performance is structure-sensitive and species-specific. Increasing structural complexity does not systematically improve fit; instead, performance depends more on choosing the appropriate subfunction family than on within-family flexibility (Samanta et al., 2008; Whitley et al., 2013). This highlights that reliable modeling of *SFD* and its environmental responses requires both the fitting of parameters and the selection of physiologically appropriate response structures. Our framework addresses these needs: the flexible and interpretable Jarvis-type model accommodates alternative response functions and additional terms, while Bayesian inference supports probabilistic parameter estimation, allows the upper-bound term to be modeled hierarchically across sites, and quantifies parameter uncertainty.

The dominant source of structural sensitivity differs between species (Supplementary Data). In *T. cordata*, allowing soil-moisture penalties

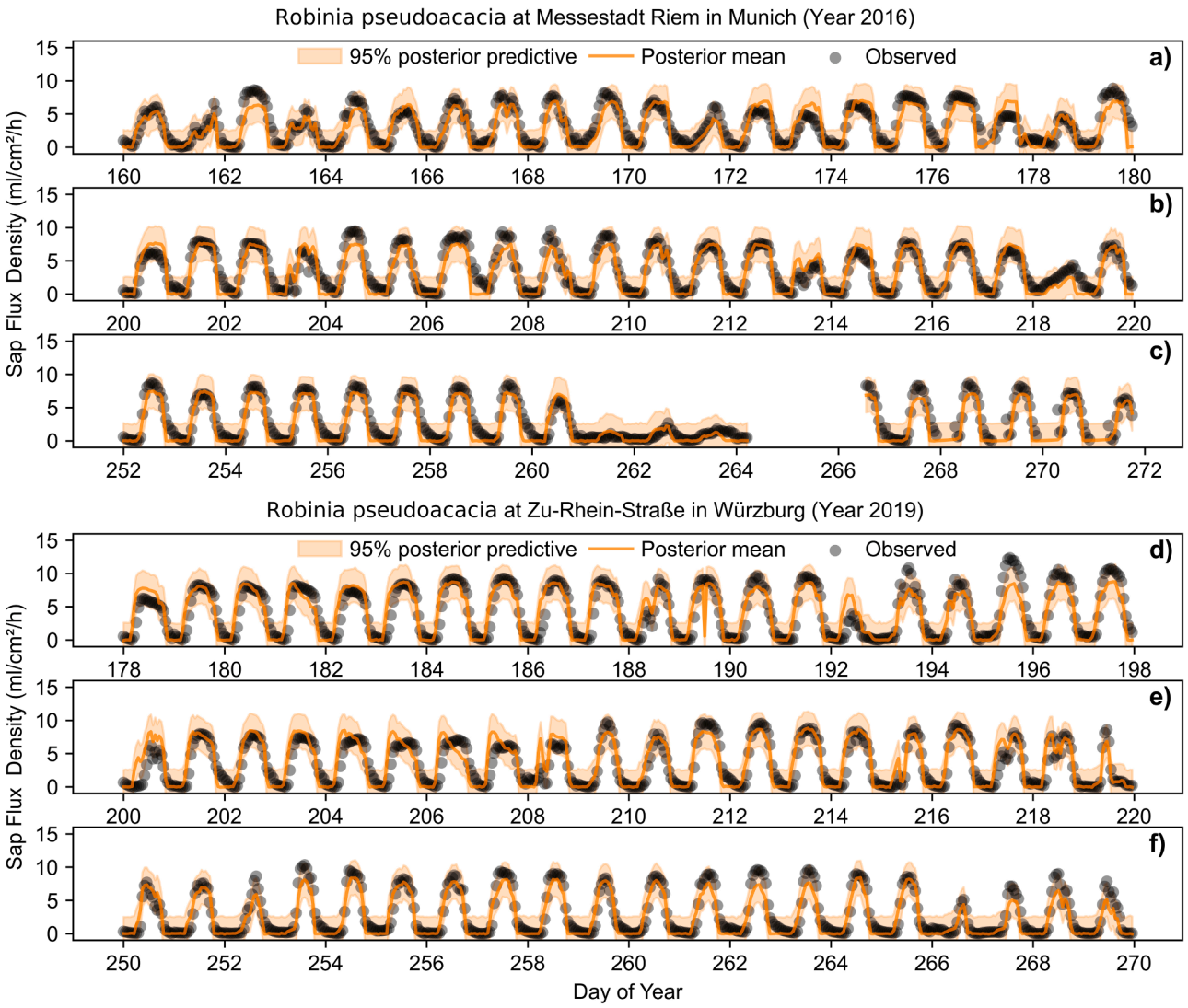

Fig. 7. Posterior predictive distributions of *SFD* for *R. pseudoacacia*, generated using an HBM with the optimal Jarvis configuration: $F^2(R_s)\cdot F^2(T_a)\cdot F^1(VPD)\cdot F^1(\theta)\cdot F(DOY)$.

$F^{2,3}(\theta)$ markedly improves fit over $F^1(\theta)$ (mean WAIC from −3529.52 to −6491.07). In *R. pseudoacacia*, a rise-then-decline $F^1(VPD)$ captures the pre-downturn increase and improves fit (−1374.86 to −1931.39). Once these key subfunctions are fixed, replacing $F(T_a)$ or $F(R_s)$ has little influence on performance. Structural uncertainty is therefore not uniform across drivers, but organized around species-specific controlling responses. Comparison across the baseline, hierarchical, and seasonal formulations further suggests that empirical Jarvis parameters are specification-dependent rather than fixed constants. We therefore interpret the baseline model primarily in terms of environmental response structure, whereas the hierarchical and seasonal variants are more appropriate for estimation under heterogeneous urban conditions. Within the temperate Bavarian domain, a cautious conclusion is that a shared atmospheric-response structure $F^2(R_s)\cdot F^2(T_a)\cdot F^1(VPD)$ can transfer across species after re-estimation, whereas $F(\theta)$ remains species-specific and context-dependent.

4.4. Urban applicability and limitations of the framework

From a management perspective, the contrasting behavior of the two species suggests different priorities under urban heat and drought stress. For *T. cordata*, sustaining its higher latent-cooling potential requires adequate soil water supply, and this potential is reduced when water availability declines. Closer monitoring, together with timely irrigation, may therefore help sustain this potential. By contrast, *R. pseudoacacia* may be better suited to sites with less reliable shallow soil water availability, although this advantage may be offset under high atmospheric demand because earlier regulation can limit transpiration. These contrasts should be considered in species selection, irrigation planning, and the parameterization of tree transpiration in urban microclimate models.

The framework is suitable for prediction in principle, but the present study focuses on inference and cross-species comparison rather than forecasting. More broadly, the framework can be refitted in other cities or climatic contexts given comparable sap flux and environmental observations, allowing species-specific environmental responses and transpiration potential to be evaluated locally. For similar climatic domains, the present species-level conclusions may be more directly informative; otherwise, direct parameter transfer should be avoided. Extending the framework to warmer future conditions with more frequent heatwaves and droughts will be an important next step.

Our results highlight both the promise and limits of trait-based parameterization. The observed interspecific differences are qualitatively consistent with known hydraulic strategies, but no direct trait-parameter mapping is possible within the present Jarvis-type

framework; any quantitative linkage would require independently measured trait data or a more explicitly hydraulic model (Buckley, 2019). Future work could therefore test hydraulic trait-informed predictors, such as wood density or leaf turgor-loss point (Dekker et al., 2000), and, where warranted, add targeted Jarvis stress terms (Chen et al., 2020).

In addition, while the shallow θ used here provides a consistent cross-site indicator, future work could strengthen the representation of tree soil-water responses by incorporating layered soil moisture profiles or deeper observations (Harper et al., 2021). The current $F(DOY)$ formulation may be more applicable to the temperate deciduous context examined here and may require adaptation in systems with different seasonal rhythms. Finally, residual within-species variation may reflect tree-level attributes, site-specific conditions, and microclimatic variables such as wind speed that were not fully resolved in the current dataset, suggesting the need for broader field monitoring in urban contexts.

5. Conclusion

This study uses hourly observations from nine urban sites in Munich and Würzburg (2015–2021) to quantify parameter and structural uncertainty in species-specific Jarvis models for *T. cordata* and *R. pseudoacacia*, screening 81 subfunction configurations and embedding the best-performing structures in a hierarchical Bayesian framework with a seasonal term. Species differed in both environmental responses and dominant structural sensitivities: soil-moisture subfunction choice was most influential for *T. cordata*, whereas *VPD* subfunction choice dominated for *R. pseudoacacia*, showing that species-specific Jarvis modeling requires both appropriate subfunction selection and parameter calibration. Hierarchical site effects and seasonal representation further improved estimation across heterogeneous urban sites, supporting species-explicit representation of urban tree water use in microclimate models.

CRediT authorship contribution statement

Xiang Zhang: Conceptualization, Formal analysis, Funding acquisition, Methodology, Project administration, Resources, Software, Visualization, Writing – original draft, Writing – review & editing. **Xue Zhong:** Conceptualization, Funding acquisition, Methodology, Writing – original draft. **Jun-Ru Yan:** Conceptualization, Formal analysis, Writing – review & editing. **Qi Li:** Conceptualization, Formal analysis, Writing – review & editing. **Ling-Ye Yao:** Conceptualization, Methodology, Writing – review & editing. **Kai-Xin Liu:** Conceptualization, Visualization, Writing – original draft. **Astrid Moser-Reischl:** Conceptualization, Data curation, Investigation, Project administration, Writing – review & editing. **Thomas Rötzer:** Conceptualization, Data curation, Funding acquisition, Investigation, Project administration, Resources, Supervision, Writing – review & editing. **Stephan Pauleit:** Conceptualization, Data curation, Funding acquisition, Project administration, Supervision. **Mohammad A. Rahman:** Conceptualization, Data curation, Formal analysis, Funding acquisition, Investigation, Methodology, Project administration, Resources, Supervision, Writing – review & editing.

Declaration of competing interest

The authors declare that they have no known competing financial interests or personal relationships that could have appeared to influence the work reported in this paper.

Acknowledgements

This work was supported by the Alexander von Humboldt Fellowship; Trait-Based Assessment of Urban Tree Health and Climate Resilience, funded by TREE Fund (#25-JK-01); Climate Experience Würzburg: Influence of Trees on the Microclimate of the City of Würzburg (TKP01KPB-71924) within the Center for Urban Ecology and Climate Adaptation funded by the Bavarian State Ministry of the Environment and Consumer Protection; the German Research Foundation through the project CUT-Climate and Urban Trees: Effects of Trees on Urban Climates during Climate Change (PA 2626/3-1, PR 292/21-1); the National Natural Science Foundation of China (No. 32501726); the China Postdoctoral Science Foundation Postdoctoral Fellowship Program (No. GZC20251115); and the China Scholarship Council (No. 202306150006). We thank the Department for Municipal Green Areas of Munich and the relevant municipal authorities in Würzburg for their support, and we are grateful to all colleagues and field assistants for their dedicated efforts in instrumentation, maintenance, and data collection.

Supplementary materials

Supplementary material associated with this article can be found, in the online version, at doi:10.1016/j.agrformet.2026.111381.

Data availability

Data will be made available on request.

References

Anys, M., Weiler, M., 2025. Controls on tree transpiration dynamics in an urban environment. Agric. For. Meteorol. 372, 110726. https://doi.org/10.1016/j.agrformet.2025.110726.

Barros, F., de, V., Bittencourt, P.R.L., Brum, M., Restrepo-Coupe, N., Pereira, L., Teodoro, G.S., Saleska, S.R., Borma, L.S., Christoffersen, B.O., Penha, D., Alves, L.F., Lima, A.J.N., Carneiro, V.M.C., Gentine, P., Lee, J.-E., Aragão, L.E.O.C., Ivanov, V., Leal, L.S.M., Araujo, A.C., Oliveira, R.S., 2019. Hydraulic traits explain differential responses of amazonian forests to the 2015 el niño-induced drought. New Phytol. 223, 1253–1266. https://doi.org/10.1111/nph.15909.

Buccolieri, R., Santiago, J.-L., Rivas, E., Sanchez, B., 2018. Review on urban tree modelling in CFD simulations: aerodynamic, deposition and thermal effects. Urban For. Urban Green. 31, 212–220. https://doi.org/10.1016/j.ufug.2018.03.003.

Buckley, T.N., 2019. How do stomata respond to water status? New Phytol. 224, 21–36. https://doi.org/10.1111/nph.15899.

Buckley, T.N., Turnbull, T.L., Adams, M.A., 2012. Simple models for stomatal conductance derived from a process model: cross-validation against sap flux data. Plant Cell Environ. 35, 1647–1662. https://doi.org/10.1111/j.1365-3040.2012.02515.x.

Chen, D., Hsu, K., Duan, X., Wang, Y., Wei, X., Muhammad, S., 2020. Bayesian analysis of jujube canopy transpiration models: does embedding the key environmental factor in jarvis canopy resistance sub-model always associate with improving transpiration modeling? Agric. Water Manage. 234, 106112. https://doi.org/10.1016/j.agwat.2020.106112.

Chen, H., Jiang, A.Z., Huang, J.J., Li, H., McBean, E., Singh, V.P., Zhang, J., Lan, Z., Gao, J., Zhou, Z., 2022. An enhanced shuttleworth-wallace model for simulation of evapotranspiration and its components. Agric. For. Meteorol. 313, 108769. https://doi.org/10.1016/j.agrformet.2021.108769.

Cierjacks, A., Kowarik, I., Joshi, J., Hempel, S., Ristow, M., von der Lippe, M., Weber, E., 2013. Biological Flora of the British Isles: robinia pseudoacacia. J. Ecol. 101, 1623–1640. https://doi.org/10.1111/1365-2745.12162.

Clark, J.S., 2005. Why environmental scientists are becoming bayesians. Ecol. Lett. 8, 2–14. https://doi.org/10.1111/j.1461-0248.2004.00702.x.

Clausnitzer, F., Köstner, B., Schwärzel, K., Bernhofer, C., 2011. Relationships between canopy transpiration, atmospheric conditions and soil water availability—analyses of long-term sap-flow measurements in an old norway spruce forest at the ore mountains/germany. Agric. For. Meteorol. 151, 1023–1034. https://doi.org/10.1016/j.agrformet.2011.04.007.

Damour, G., Simonneau, T., Cochard, H., Urban, L., 2010. An overview of models of stomatal conductance at the leaf level. Plant Cell Environ. 33. https://doi.org/10.1111/j.1365-3040.2010.02181.x no–no.

Deans, R.M., Brodribb, T.J., Busch, F.A., Farquhar, G.D., 2019. Plant water-use strategy mediates stomatal effects on the light induction of photosynthesis. New Phytol. 222, 382–395. https://doi.org/10.1111/nph.15572.

Dekker, S.C., Bouten, W., Verstraten, J.M., 2000. Modelling forest transpiration from different perspectives. Hydrol. Process. 14, 251–260. https://doi.org/10.1002/(SICI)1099-1085(20000215)14:2%3C251::AID-HYP923%3E3.0.CO;2-R.

Delzon, S., Loustau, D., 2005. Age-related decline in stand water use: sap flow and transpiration in a pine forest chronosequence. Agric. For. Meteorol. 129, 105–119. https://doi.org/10.1016/j.agrformet.2005.01.002.

Feng, X., Dietze, M., 2013. Scale dependence in the effects of leaf ecophysiological traits on photosynthesis: bayesian parameterization of photosynthesis models. New Phytol. 200, 1132–1144. https://doi.org/10.1111/nph.12454.

Fuchs, S., Leuschner, C., Mathias Link, R., Schuldt, B., 2021. Hydraulic variability of three temperate broadleaf tree species along a water availability gradient in central europe. New Phytol. 231, 1387–1400. https://doi.org/10.1111/nph.17448.
Ganguly, A.R., Steinhaeuser, K., Erickson, D.J., Branstetter, M., Parish, E.S., Singh, N., Drake, J.B., Buja, L., 2009. Higher trends but larger uncertainty and geographic variability in 21st century temperature and heat waves. Proc. Natl. Acad. Sci. 106, 15555–15559. https://doi.org/10.1073/pnas.0904495106.
Gelman, A., 2006. Prior distributions for variance parameters in hierarchical models (comment on article by browne and draper). Bayesian Anal. 1, 515–534. https://doi.org/10.1214/06-BA117A.
Gelman, A., Carlin, J.B., Stern, H.S., Dunson, D.B., Vehtari, A., Rubin, D.B., 2013. Bayesian Data Analysis, 3rd ed. Chapman and Hall/CRC, New York. https://doi.org/10.1201/b16018.
Gelman, A., Hwang, J., Vehtari, A., 2014. Understanding predictive information criteria for bayesian models. Stat. Comput. 24, 997–1016. https://doi.org/10.1007/s11222-013-9416-2.
Gobatti, L., Bach, P.M., Maurer, M., Leitão, J.P., 2025. Impact of soil moisture content on urban tree evaporative cooling and human thermal comfort. Npj Urban Sustain. 5, 26. https://doi.org/10.1038/s42949-025-00220-0.
Granier, A., 1987. Evaluation of transpiration in a douglas-fir stand by means of sap flow measurements. Tree Physiol. 3, 309–320. https://doi.org/10.1093/treephys/3.4.309.
Granier, A., Reichstein, M., Bréda, N., Janssens, I.A., Falge, E., Ciais, P., Grünwald, T., Aubinet, M., Berbigier, P., Bernhofer, C., Buchmann, N., Facini, O., Grassi, G., Heinesch, B., Ilvesniemi, H., Keronen, P., Knohl, A., Köstner, B., Lagergren, F., Lindroth, A., Longdoz, B., Loustau, D., Mateus, J., Montagnani, L., Nys, C., Moors, E., Papale, D., Peiffer, M., Pilegaard, K., Pita, G., Pumpanen, J., Rambal, S., Rebmann, C., Rodrigues, A., Seufert, G., Tenhunen, J., Vesala, T., Wang, Q., 2007. Evidence for soil water control on carbon and water dynamics in european forests during the extremely dry year: 2003. Agric. For. Meteorol. 143, 123–145. https://doi.org/10.1016/j.agrformet.2006.12.004.
Granier, A., Loustau, D., 1994. Measuring and modelling the transpiration of a maritime pine canopy from sap-flow data. Agric. For. Meteorol. 71, 61–81. https://doi.org/10.1016/0168-1923(94)90100-7.
Gregg, J.W., Jones, C.G., Dawson, T.E., 2003. Urbanization effects on tree growth in the vicinity of new york city. Nature 424, 183–187. https://doi.org/10.1038/nature01728.
Grossiord, C., Buckley, T.N., Cernusak, L.A., Novick, K.A., Poulter, B., Siegwolf, R.T.W., Sperry, J.S., McDowell, N.G., 2020. Plant responses to rising vapor pressure deficit. New Phytol. 226, 1550–1566. https://doi.org/10.1111/nph.16485.
Harper, A.B., Williams, K.E., McGuire, P.C., Duran Rojas, M.C., Hemming, D., Verhoef, A., Huntingford, C., Rowland, L., Marthews, T., Breder Eller, C., Mathison, C., Nobrega, R.L.B., Gedney, N., Vidale, P.L., Otu-Larbi, F., Pandey, D., Garrigues, S., Wright, A., Slevin, D., De Kauwe, M.G., Blyth, E., Ardö, J., Black, A., Bonal, D., Buchmann, N., Burban, B., Fuchs, K., de Grandcourt, A., Mammarella, I., Merbold, L., Montagnani, L., Nouvellon, Y., Restrepo-Coupe, N., Wohlfahrt, G., 2021. Improvement of modeling plant responses to low soil moisture in JULESvn4.9 and evaluation against flux tower measurements. Geosci. Model Dev. 14, 3269–3294. https://doi.org/10.5194/gmd-14-3269-2021.
Hastings, W.K., 1970. Monte carlo sampling methods using markov chains and their applications. Biometrika 57, 97–109. https://doi.org/10.1093/biomet/57.1.97.
Hill, B.M., 1974. Bayesian inference in statistical analysis. Technometrics 16, 478–479. https://doi.org/10.1080/00401706.1974.10489222.
Hoffman, M.D., Gelman, A., 2011. The No-U-turn sampler: adaptively setting path lengths in Hamiltonian Monte Carlo. https://doi.org/10.48550/arXiv.1111.4246.
Huang, Y., Li, X., Zhang, Z., He, C., Zhao, P., You, Y., Mo, L., 2011. Seasonal changes in *cyclobalanopsis glauca* transpiration and canopy stomatal conductance and their dependence on subterranean water and climatic factors in rocky karst terrain. J. Hydrol. 402, 135–143. https://doi.org/10.1016/j.jhydrol.2011.03.013.
Jarvis, P.G., 1976. The interpretation of the variations in leaf water potential and stomatal conductance found in canopies in the field. Philos. Trans. R. Soc. Lond. B Biol. Sci. 273, 593–610. https://doi.org/10.1098/rstb.1976.0035.
Kajosaari, A., Hasanzadeh, K., Fagerholm, N., Nummi, P., Kuusisto-Hjort, P., Kyttä, M., 2024. Predicting context-sensitive urban green space quality to support urban green infrastructure planning. Landscape Urban Plann. 242, 104952. https://doi.org/10.1016/j.landurbplan.2023.104952.
Kato, T., Kimura, R., Kamichika, M., 2004. Estimation of evapotranspiration, transpiration ratio and water-use efficiency from a sparse canopy using a compartment model. Agric. Water Manage. 65, 173–191. https://doi.org/10.1016/j.agwat.2003.10.001.
Kelleher, C., Wagener, T., McGlynn, B., Ward, A.S., Gooseff, M.N., Payn, R.A., 2013. Identifiability of transient storage model parameters along a mountain stream. Water Resour. Res. 49, 5290–5306. https://doi.org/10.1002/wrcr.20413.
Kjelgren, R.K., Clark, J.R., 1992. Microclimates and tree growth in three urban spaces. J. Environ. Hortic. 10, 139–145. https://doi.org/10.24266/0738-2898-10.3.139.
Kume, T., Komatsu, H., Kuraji, K., Suzuki, M., 2008. <20-min time lags between transpiration and stem sap flow in emergent trees in a bornean tropical rainforest. Agric. For. Meteorol. 148, 1181–1189. https://doi.org/10.1016/j.agrformet.2008.02.010.
Leigh, A., Sevanto, S., Close, J.d., Nicotra, A.b., 2017. The influence of leaf size and shape on leaf thermal dynamics: does theory hold up under natural conditions? Plant Cell Environ. 40, 237–248. https://doi.org/10.1111/pce.12857.
Li, Q., Li, Q., Peng, H., Chen, S., 2025. Study on the effect of vertical structure of urban green spaces on microclimate in guangzhou through a full year numerical simulation. Landscape Urban Plann. 260, 105370. https://doi.org/10.1016/j.landurbplan.2025.105370.
Li, Q., Li, Qi, Mi, J., Wu, H., 2024a. A three-layer evapotranspiration model considering the vertical structure of urban green spaces. Urban for. Urban Green. 98, 128389. https://doi.org/10.1016/j.ufug.2024.128389.
Li, R., Zhao, Y., Chang, M., Zeng, F., Wu, Y., Wang, L., Niu (Leon), J., Shi, X., Gao, N., 2024b. Numerical simulation methods of tree effects on microclimate: a review. Renew. Sustain. Energy Rev. 205, 114852. https://doi.org/10.1016/j.rser.2024.114852.
Li, Q., Wang, Z.-H., 2018. Large-eddy simulation of the impact of urban trees on momentum and heat fluxes. Agric. For. Meteorol. 255, 44–56. https://doi.org/10.1016/j.agrformet.2017.07.011. Honoring W.J. Massman's Discoveries: Bringing Physics to Agriculture.
Mackay, D.S., Ewers, B.E., Loranty, M.M., Kruger, E.L., Samanta, S., 2012. Bayesian analysis of canopy transpiration models: a test of posterior parameter means against measurements. J. Hydrol. 432-433, 75–83. https://doi.org/10.1016/j.jhydrol.2012.02.019.
Manickathan, L., Defraeye, T., Allegrini, J., Derome, D., Carmeliet, J., 2018. Parametric study of the influence of environmental factors and tree properties on the transpirative cooling effect of trees. Agric. For. Meteorol. 248, 259–274. https://doi.org/10.1016/j.agrformet.2017.10.014.
Mitchell, P.J., Veneklaas, E., Lambers, H., Burgess, S.S.O., 2009. Partitioning of evapotranspiration in a semi-arid eucalypt woodland in south-western. Australia. Agric. For. Meteorol. 149, 25–37. https://doi.org/10.1016/j.agrformet.2008.07.008.
Monteith, J., Unsworth, M., 2013. Principles of Environmental physics: plants, animals, and the Atmosphere. Academic Press.
Moore, G., Macklin, J., DeCesare, L., 2010. A brief history of asa gray's manual of botany. Harvard Pap. Botan. 15, 277–286. https://doi.org/10.3100/025.015.0207.
Moser-Reischl, A., Franceschi, E., Rahman, M.A., Rodrigues-Leite, J., Pretzsch, H., Pauleit, S., Rötzer, T., 2025. Spatial and temporal dynamics of the leaf area index (LAI) of selected tree species in urban environments. Urban For. Urban Green. 107, 128795. https://doi.org/10.1016/j.ufug.2025.128795.
Moser-Reischl, A., Rahman, M.A., Pauleit, S., Pretzsch, H., Rötzer, T., 2019. Growth patterns and effects of urban micro-climate on two physiologically contrasting urban tree species. Landscape Urban Plann. 183, 88–99. https://doi.org/10.1016/j.landurbplan.2018.11.004.
Niyogi, D., Alapaty, K., Raman, S., Chen, F., 2009. Development and evaluation of a coupled photosynthesis-based gas exchange evapotranspiration model (GEM) for mesoscale weather forecasting applications. https://doi.org/10.1175/2008JAMC1662.1.
Nossent, J., Elsen, P., Bauwens, W., 2011. Sobol' sensitivity analysis of a complex environmental model. Environ. Modell. Software 26, 1515–1525. https://doi.org/10.1016/j.envsoft.2011.08.010.
Oke, T.R., Mills, G., Christen, A., Voogt, J.A., 2017. Urban Climates. Cambridge University Press.
Oren, R., Sperry, J.S., Katul, G.G., Pataki, D.E., Ewers, B.E., Phillips, N., Schäfer, K.V.R., 1999. Survey and synthesis of intra- and interspecific variation in stomatal sensitivity to vapour pressure deficit. Plant Cell Environ. 22, 1515–1526. https://doi.org/10.1046/j.1365-3040.1999.00513.x.
Ortega-Farias, S., Poblete-Echeverría, C., Brisson, N., 2010. Parameterization of a two-layer model for estimating vineyard evapotranspiration using meteorological measurements. Agric. For. Meteorol. 150, 276–286. https://doi.org/10.1016/j.agrformet.2009.11.012.
Panchen, Z.A., Primack, R.B., Nordt, B., Ellwood, E.R., Stevens, A.-D., Renner, S.S., Willis, C.G., Fahey, R., Whittemore, A., Du, Y., Davis, C.C., 2014. Leaf out times of temperate woody plants are related to phylogeny, deciduousness, growth habit and wood anatomy. New Phytol. 203, 1208–1219. https://doi.org/10.1111/nph.12892.
Paschalis, A., De Kauwe, M.G., Sabot, M., Fatichi, S., 2024. When do plant hydraulics matter in terrestrial biosphere modelling? Global Change Biol. 30, e17022. https://doi.org/10.1111/gcb.17022.
Peters, R.L., Arend, M., Zahnd, C., Hoch, G., Arndt, S.K., Cernusak, L.A., Poyatos, R., Zhorzel, T., Kahmen, A., 2025. Uniform regulation of stomatal closure across temperate tree species to sustain nocturnal turgor and growth. Nat. Plants 11, 725–730. https://doi.org/10.1038/s41477-025-01957-3.
Piironen, J., Vehtari, A., 2017. Comparison of bayesian predictive methods for model selection. Stat. Comput. 27, 711–735. https://doi.org/10.1007/s11222-016-9649-y.
Poyatos, R., Villagarcía, L., Domingo, F., Piñol, J., Llorens, P., 2007. Modelling evapotranspiration in a scots pine stand under mediterranean mountain climate using the GLUE methodology. Agric. For. Meteorol. 146, 13–28. https://doi.org/10.1016/j.agrformet.2007.05.003.
Rahman, M.A., Arndt, S., Bravo, F., Cheung, P.K., van Doorn, N., Franceschi, E., del Río, M., Livesley, S.J., Moser-Reischl, A., Pattnaik, N., Rötzer, T., Paeth, H., Pauleit, S., Preisler, Y., Pretzsch, H., Tan, P.Y., Cohen, S., Szota, C., Torquato, P.R., 2024. More than a canopy cover metric: influence of canopy quality, water-use strategies and site climate on urban forest cooling potential. Landscape Urban Plann. 248, 105089. https://doi.org/10.1016/j.landurbplan.2024.105089.
Rahman, M.A., Moser, A., Anderson, M., Zhang, C., Rötzer, T., Pauleit, S., 2019. Comparing the infiltration potentials of soils beneath the canopies of two contrasting urban tree species. Urban For. Urban Green. 38, 22–32. https://doi.org/10.1016/j.ufug.2018.11.002.
Rahman, M.A., Moser, A., Gold, A., Rötzer, T., Pauleit, S., 2018. Vertical air temperature gradients under the shade of two contrasting urban tree species during different types of summer days. Sci. Total Environ. 633, 100–111. https://doi.org/10.1016/j.scitotenv.2018.03.168.
Rahman, M.A., Moser, A., Rötzer, T., Pauleit, S., 2017a. Microclimatic differences and their influence on transpirational cooling of *tilia cordata* in two contrasting street

canyons in Munich, Germany. Agric. For. Meteorol. 232, 443–456. https://doi.org/10.1016/j.agrformet.2016.10.006.
Rahman, M.A., Moser, A., Rötzer, T., Pauleit, S., 2017b. Within canopy temperature differences and cooling ability of *tilia cordata* trees grown in urban conditions. Build. Environ. 114, 118–128. https://doi.org/10.1016/j.buildenv.2016.12.013.
Rötzer, T., Moser-Reischl, A., Rahman, M.A., Hartmann, C., Paeth, H., Pauleit, S., Pretzsch, H., 2021. Urban tree growth and ecosystem services under extreme drought. Agric. For. Meteorol. 308-309, 108532. https://doi.org/10.1016/j.agrformet.2021.108532.
Samanta, S., Clayton, M.K., Mackay, D.S., Kruger, E.L., Ewers, B.E., 2008. Quantitative comparison of canopy conductance models using a bayesian approach. Water Resour. Res. 44. https://doi.org/10.1029/2007WR006761.
Samanta, S., Mackay, D.S., Clayton, M.K., Kruger, E.L., Ewers, B.E., 2007. Bayesian analysis for uncertainty estimation of a canopy transpiration model. Water Resour. Res. 43. https://doi.org/10.1029/2006WR005028.
Schäfer, K.V.R., Oren, R., Tenhunen, J.D., 2000. The effect of tree height on crown level stomatal conductance. Plant Cell Environ. 23, 365–375. https://doi.org/10.1046/j.1365-3040.2000.00553.x.
Sánchez-Costa, E., Poyatos, R., Sabaté, S., 2015. Contrasting growth and water use strategies in four co-occurring mediterranean tree species revealed by concurrent measurements of sap flow and stem diameter variations. Agric. For. Meteorol. 207, 24–37. https://doi.org/10.1016/j.agrformet.2015.03.012.
Sobol′, I.M., 2001. Global sensitivity indices for nonlinear mathematical models and their monte carlo estimates. Math. Comput. Simul. 55, 271–280. https://doi.org/10.1016/S0378-4754(00)00270-6. The Second IMACS Seminar on Monte Carlo Methods.
Stewart, J.B., 1988. Modelling surface conductance of pine forest. Agric. For. Meteorol. 43, 19–35. https://doi.org/10.1016/0168-1923(88)90003-2.
Tabassum, S., Ossola, A., Marchin, R.M., Ellsworth, D.S., Leishman, M.R., 2021. Assessing the relationship between trait-based and horticultural classifications of plant responses to drought. Urban for. Urban Green. 61, 127109. https://doi.org/10.1016/j.ufug.2021.127109.
Torres-Ruiz, J.M., Cochard, H., Delzon, S., Boivin, T., Burlett, R., Cailleret, M., Corso, D., Delmas, C.E.L., De Caceres, M., Diaz-Espejo, A., Fernández-Conradi, P., Guillemot, J., Lamarque, L.J., Limousin, J.-M., Mantova, M., Mencuccini, M., Morin, X., Pimont, F., De Dios, V.R., Ruffault, J., Trueba, S., Martin-StPaul, N.K., 2024. Plant hydraulics at the heart of plant, crops and ecosystem functions in the face of climate change. New Phytol. 241, 984–999. https://doi.org/10.1111/nph.19463.
Tyree, M.T., Ewers, F.W., 1991. The hydraulic architecture of trees and other woody plants. New Phytol. 119, 345–360. https://doi.org/10.1111/j.1469-8137.1991.tb00035.x.
Van Hoey, S., Seuntjens, P., van der Kwast, J., Nopens, I., 2014. A qualitative model structure sensitivity analysis method to support model selection. J. Hydrol. 519, 3426–3435. https://doi.org/10.1016/j.jhydrol.2014.09.052.
Vehtari, A., Gelman, A., Gabry, J., 2017. Practical bayesian model evaluation using leave-one-out cross-validation and WAIC. Stat. Comput. 27, 1413–1432. https://doi.org/10.1007/s11222-016-9696-4.
Vehtari, A., Gelman, A., Simpson, D., Carpenter, B., Bürkner, P.-C., 2021. Rank-normalization, folding, and localization: an improved r̂ for assessing convergence of MCMC (with discussion). Bayesian Anal. 16, 667–718. https://doi.org/10.1214/20-BA1221.
Verhoef, A., Egea, G., 2014. Modeling plant transpiration under limited soil water: comparison of different plant and soil hydraulic parameterizations and preliminary implications for their use in land surface models. Agric. For. Meteorol. 191, 22–32. https://doi.org/10.1016/j.agrformet.2014.02.009.
Wang, H., Guan, H., Liu, N., Soulsby, C., Tetzlaff, D., Zhang, X., 2020. Improving the jarvis-type model with modified temperature and radiation functions for sap flow simulations. J. Hydrol. 587, 124981. https://doi.org/10.1016/j.jhydrol.2020.124981.
Wang, H., Guan, H., Simmons, C.T., 2016. Modeling the environmental controls on tree water use at different temporal scales. Agric. For. Meteorol. 225, 24–35. https://doi.org/10.1016/j.agrformet.2016.04.016.
Wang, H., Tetzlaff, D., Dick, J.J., Soulsby, C., 2017. Assessing the environmental controls on scots pine transpiration and the implications for water partitioning in a boreal headwater catchment. Agric. For. Meteorol. 240-241, 58–66. https://doi.org/10.1016/j.agrformet.2017.04.002.
Wang, H., Tetzlaff, D., Soulsby, C., 2019. Hysteretic response of sap flow in scots pine (pinus sylvestris) to meteorological forcing in a humid low-energy headwater catchment. Ecohydrology 12, e2125. https://doi.org/10.1002/eco.2125.
Whitley, R., Taylor, D., Macinnis-Ng, C., Zeppel, M., Yunusa, I., O'Grady, A., Froend, R., Medlyn, B., Eamus, D., 2013. Developing an empirical model of canopy water flux describing the common response of transpiration to solar radiation and VPD across five contrasting woodlands and forests. Hydrol. Process. 27, 1133–1146. https://doi.org/10.1002/hyp.9280.
Yang, Y., Gatto, E., Gao, Z., Buccolieri, R., Morakinyo, T.E., Lan, H., 2019. The "plant evaluation model" for the assessment of the impact of vegetation on outdoor microclimate in the urban environment. Build. Environ. 159, 106151. https://doi.org/10.1016/j.buildenv.2019.05.029.
Zepp, H., Gessner, M., Gruenhagen, L., Bührs, M., 2023. Modeling the cooling effect of urban green spaces: the neglected control variables of 'soil moisture' and 'biotope types'. Urban for. Urban Green. 90, 128137. https://doi.org/10.1016/j.ufug.2023.128137.
Zhang, X., Ren, P., Yao, L.-Y., Li, Q., Zhong, X., Liu, K.-X., Guo, T.-Y., Yang, J.-H., Zhao, L.-H., Pauleit, S., Rahman, M.A., 2025. Investigating tree shading and thermal variations in a subtropical zone: single tree to urban squares. Build. Environ. 283, 113408. https://doi.org/10.1016/j.buildenv.2025.113408.
Zhang, X., Zhao, L., Yao, L., Zhong, X., Ren, P., 2022. Investigating the micro-scale thermal effects of natural underlying surfaces on adjacent spaces in a subtropical zone with an optimized method. Build. Environ. 222, 109382. https://doi.org/10.1016/j.buildenv.2022.109382.
Zhou, Z., Wang, Y., An, Z., Li, R., Xu, Y., Zhang, P., Yang, Y., Wang, T., 2022. Deep root information "hidden in the dark": a case study on the 21-m soil profile of *robinia pseudoacacia* in the critical zone of the chinese loess plateau. Catena 213, 106121. https://doi.org/10.1016/j.catena.2022.106121.
Zhu, G., Su, Y., Li, X., Zhang, K., Li, C., 2013. Estimating actual evapotranspiration from an alpine grassland on qinghai-tibetan plateau using a two-source model and parameter uncertainty analysis by bayesian approach. J. Hydrol. 476, 42–51. https://doi.org/10.1016/j.jhydrol.2012.10.006.